博士論文（要約）

Analysis and Calibration Techniques of Modulated Wideband Converter for High-Precision Sub-Nyquist Sampling System

（高精度サブナイキストサンプリングシステムのための
変調広帯域変換器の解析と補正技術）

A Dissertation
Submitted to the Department of
Electrical Engineering and
Information Systems,
the University of Tokyo
in Partial Fulfillment of the Requirements
for the Degree of Doctor of Philosophy

Supervisor: Professor Tetsuya Iizuka

Zolboo Byambadorj

ビャムバドルジ ゾルボー

Department of Electrical Engineering and Information Systems

The University of Tokyo

December 2020

Abstract

This thesis focuses on analysis and calibration techniques of the modulated wideband converter (MWC) for a high-precision sub-Nyquist sampling system. We address the theoretical analysis of the noise figure for the MWC to facilitate the system-level optimization of the MWC-based receiver architectures. An advanced digital compensation filter is proposed to fix a non-ideal frequency characteristic of the practical MWC. We also propose a novel calibration technique for simultaneous estimation of actual sensing matrix coefficients on the MWC.

Chapter 2 covers brief mathematical backgrounds of the MWC system, which is contributed by other researchers. The main framework of the MWC relies on compressed sensing theory. The perfect reconstruction is guaranteed under an ideal situation. We also summarized the recent practical challenges of the MWC in this Chapter.

Chapter 3 focuses on creating the MWC platform on MATLAB. The waveform reconstruction capability of the MWC was demonstrated based on the MATLAB platform for variously chosen design parameters. When the wideband signal is not clean sparse, the sidebands should be considered for the reconstruction to improve the performance.

Chapter 4 investigates a comprehensive analytical definition of the noise figure (NF) on MWC systems, including the reconstruction process in the digital domain. The first contribution of this Chapter is a part-by-part definition of the NF on MWC systems and its dependence on design properties. The next contribution is the average noise figure to evaluate the noise performance of the MWC upon all carrier frequencies based on its design parameters. The proposed analysis will provide an analytical expression of the NF

of the MWC system based on its design parameters, which can be utilized to predict and optimize the noise performance of the MWC considering the performance trade-offs such as power consumption and hardware cost. It must also be useful to guide the appropriate choice for the entire receiver systems' building blocks, including analog front ends.

Chapter 6 proposes a novel calibration method for simultaneous estimation of all the components of the actual sensing matrix based on a single measurement with a non-sparse multi-tones signal. Not only the number of measurements is reduced in the proposed method, but also the impact of the measurement-to-measurement timing fluctuations on the calibrated sensing matrix is fundamentally suppressed. The performance of the proposed calibration method is demonstrated in terms of normalized mean square error (NMSE) and image rejection ratio (IRR) for the reconstruction of the original time-domain waveform.

In Chapter 8, conclusions are made, and future works are mentioned.

The results in this thesis, such as the theoretical noise analysis, the advanced compensation filter and the calibration techniques, will be used as a guideline for practical realizations of MWC to predict the noise performance and make the high-precision time-domain waveform reconstruction.

Acknowledgments

There are many people to thank and many institutions to appreciate. It is impossible to mention all of them here. This thesis would never be able to be written without their united support, guidance and care.

First of all, I would like to thank my supervisor, Professor Tetsuya Iizuka, for his endless support, understanding, and invaluable guidance throughout my graduate study. His encouragement helped me a lot when I lost my confidence during the study. I feel truly fortunate to have studied under him.

I would like to thank Dr. Koji Asami for his excellent advice on digital signal processing and his generosity in sharing his professional experiences. His intuitive understandings and constructive idea helped me to find a solution for complex problems in the study.

I would like to express my gratitude to Prof. Makoto Ikeda for his kind advice on my progress in the joint lab meetings. His important criticisms encouraged me to perceive the big picture in this field.

I would like to express my gratitude to Advantest D2T Research Department and Systems Design Lab (d.lab), especially Prof. Akio Higo and Dr. Takahiro J. Yamaguchi. Their precious discussion on theoretical understandings of MWC leads me to more profound thoughts, which helps me understand obstacles from inside of MWC.

I further acknowledge my dissertation committee, Prof. Akira Hirose, Prof. Masahiro Fujita, Prof. Makoto Takamiya, Prof. Tadahiro Kuroda, and Prof. Masaya Miyahara, for their valuable comments and advice.

I also wish to thank the current and former lab members of Ikeda and Iizuka Labo-

ratories for their collaboration and enjoyable discussions. I am indebted in particular to my tutor Mr. Naoki Terao, for his excellent support and cheerfulness.

I would like to acknowledge the Higher Engineering Education Development (MJEED) project team for awarding me the degree program scholarship. They lightened my financial burden to study in Japan, which allowed me to concentrate more on the study.

I also would like to acknowledge the National University of Mongolia (NUM), especially to my former supervisors at NUM. During my Bachelor's study, my supervisor, Prof. Byambajav Dorj, influenced me most to pursue an academic carrier in this field. His specialized advice helped me to build the best version of myself. My supervisor in my master's study, Prof. Bayarpurev Mongol, enables studying at the University of Tokyo. His mathematical understanding and fruitful discussions inspire me so much to observe the research from a different perspective.

Finally, I would like to express my huge thanks to my parents, my older brother and his family. Without their long-distance love, I would never have had the power to pursue a doctoral degree in this field.

Contents

List of Figures

List of Tables

Chapter 1

Introduction

1.1 Background and Research Objectives

Wideband signal spectrum sensing has been successfully applied to cognitive radios and spectrum analyzers. Cognitive radio allows secondary users to opportunistically use the licensed spectrum when the corresponding band is vacant [1–3]. The traditional way for detecting such vacant bands in a wideband spectrum is channel-by-channel sequential scanning [4], which needs long sensing time. Another possible way is to use an RF front-end with a bank of narrow band-pass filters that is inefficient in terms of hardware complexity, even if it solves the latency issue. An alternative method is to directly sense a wideband signal with a very high sampling rate ADC, making the method costly and infeasible [5]. Fortunately, human-made RF signals are often sparse in the allocated band. For instance, in the wireless standard IEEE-802.11, the allocated wideband signal is centered at 2.4 GHz with several active bands depending on the surrounding users. A single band's most common demodulation method is to mix the wideband input signal by a local oscillator with the desired frequency. A low-pass filter is then applied to eliminate unwanted adjacent bands to avoid aliasing-effect in the subsequent ADC device. Afterward, the ADC is expected to sample the filter's output with the Nyquist rate, which must be equal to the bandwidth of the single channel.

To overcome the sampling rate bottleneck, a sub-Nyquist sampling system named

Modulated Wideband Converter (MWC) that uses reduced sampling rate in multi-band settings below Nyquist rate has been widely studied [6–11],tao,lexa,matusiak,wang2019,zhao. Besides, a remarkable asset is design flexibility that allows trade-off choice between each ADC sampling rate and the number of channels. The MWC can also be useful for an Automatic Test Equipment (ATE) to test devices with various frequency bands. An ATE typically has many hardware resources that include many ADCs available for analog testing. These ADCs have a slow sampling-rate but high precision in many cases. Utilizing these hardware resources, we can realize multi-channel systems to achieve effectively high sampling-rate conversion based on the MWC.

The MWC system guarantees perfect reconstruction of a wideband sparse signal based on a theory of compressed sensing [7]. Nevertheless, in the presence of noise, such as thermal noise, the impact of the noise on the reconstruction result changes significantly depending on the target carrier frequency and other system design parameters. Defining a clear explanation on the noise figure (NF) of MWC much helps in designing a complete RF receiver system that meets the target system specification. A prediction of any RF system performance demands each component's intrinsic noise and nonlinearity properties. Accordingly, to implement a practical RF receiver system that employs an MWC, it is essential to know each component's NF, IIP3 and etc.

To the best of our knowledge, previous applications of the MWC are all intended to be used for detecting power on specific frequencies without reconstructing the original time-domain waveform itself as in [12–15]. In this thesis, we will discover the high-performance possibility of the reconstruction process for the original time-domain waveform based on the MWC.

1.2 Research Objectives and Thesis Organization

This thesis focuses on analysis and calibration techniques of the modulated wideband converter (MWC) for a high-precision sub-Nyquist sampling system. We address the theoretical analysis of noise figure for the MWC in Chapter 4 to facilitate the system-

level optimization of the MWC-based receiver architectures in terms of noise performance. We propose a new method for constructing a digital compensation filter in Chapter 5 to equalize a non-ideal frequency characteristic of an analog filter. We propose novel calibration techniques for simultaneous estimation of actual sensing matrix coefficients on the MWC in Chapter 6. In Chapter 7, the actual measurement is carried out in the practical implementation to confirm the analysis and the proposed calibration techniques.

Chapter 2 covers brief mathematical backgrounds of the MWC system, which is contributed by other researchers. The main framework of the MWC relies on compressed sensing theory. The perfect reconstruction is guaranteed under an ideal situation. To the best of our knowledge, we summarized the recent practical challenges of the MWC in this Chapter.

Chapter 3 focuses on creating the MWC platform on MATLAB. Then, waveform reconstruction capability was demonstrated for variously chosen design parameters for MWC. When the wideband signal is not clean sparse, the waveform reconstruction method was proposed based on recovering sidebands in the spectrum. For example, the MWC is used for reconstructing Bluetooth signal for demonstrating its feasibility in practical signals. Jitter impacts are also investigated in the simulation environment.

Chapter 4 investigates a comprehensive analytical definition of the NF on MWC systems, including the digital domain's reconstruction process. The proposed analysis provides an analytical expression of the NF of the MWC system based on its design parameters, which can be utilized to predict and optimize the noise performance of the MWC considering the performance trade-offs such as power consumption and hardware cost. It is useful to guide the appropriate choice for the entire receiver systems' building blocks, including analog front ends.

Chapter 6 proposes a novel calibration method for simultaneous estimation of all the components of the actual sensing matrix based on a single measurement with a non-sparse pilot signal. Not only the number of measurement is reduced in the proposed method, but also the measurement-to-measurement timing fluctuations in the calibrated sensing matrix

are fundamentally suppressed. The performance of the proposed calibration method is demonstrated in terms of normalized mean square error (NMSE) and image rejection ratio (IRR) for the reconstruction of the original time-domain waveform. To the best of our knowledge, previous applications of the MWC are all intended to be used for detecting power on specific frequencies without reconstructing the original time-domain waveform itself as in [12–15]. In Chapter 6, we will discover the high-performance possibility of the reconstruction process for the time-domain waveform based on the calibration techniques of the MWC.

Chapter 7 demonstrates the measurement results of the MWC taken from the practical implementation. The noise analysis carried out in Chapter 4 is validated in this Chapter. The proposed calibration technique for the MWC in Chapter 6 estimates its actual sensing matrix coefficients with single measurements. The calibration performance has been demonstrated in NMSE and IRR, more than 50 dB and 42 dB improvement has been achieved on NMSE and IRR, respectively. Though the total number of channel mq is small as close to the necessary condition, the EVM was still under 1%, which is totally acceptable in Bluetooth device testing applications.

Finally, Chapter 8 gives conclusions of this thesis.

Chapter 2

Fundamentals of Modulated Wideband Converter

2.1 Mathematical Background

2.1.1 Wideband Sparse Signals

Frequency domain representation is useful to define a wideband sparse signal. The frequency-domain representation of a multiband signal can be modeled as

$$X(f) = \sum_{l=-L_0}^{L_0} Z_l(f - lf_p), \tag{2.1}$$

where $Z_l(f)$ is a separate spectrum slice placed at baseband, and carrier frequencies are assumed to be aligned with integer multiples of f_p here. As shown in Fig. 2.1, the frequency-shifted version of $Z_l(f)$ is sparsely placed in the frequency domain. The number of slots within the band of interest is counted as L in (2.1).

If the signal is spectrally sparse, most of $Z_l(f)$ are zero. So (2.1) is rewritten as

$$X(f) = \sum_{l \in \mathbf{S}} Z_l(f - lf_p), \tag{2.2}$$

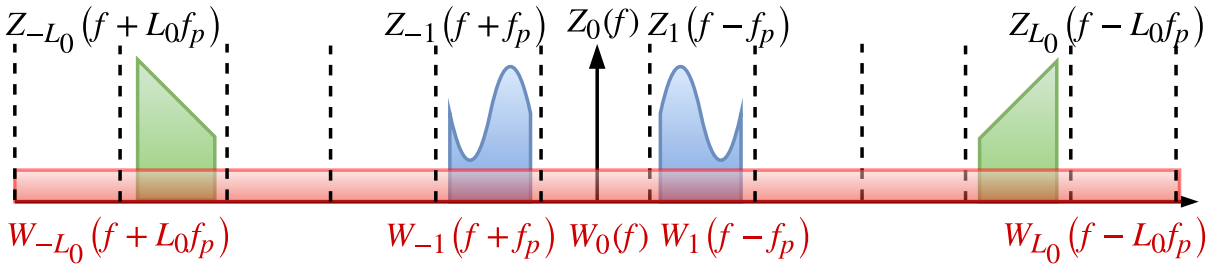

Figure 2.1: Input sparse signal spectrum model.

where $\mathbf{S}$ is a support of $X(f)$, which is a set of N indices that correspond to carrier frequencies (including conjugate frequencies) of active bands. As the signal is spectrally sparse, $N \ll L$. Furthermore, another important assumption is that each active band signal has a bandwidth B which is narrower than f_p so that any active band signals do not overlap with each other.

2.1.2 Modulated Wideband Converter (MWC)

Based on the MWC settings defined in [7], a basic and an advanced MWC are illustrated in Figs. 2.2(a) and 2.2(b), respectively. The main architecture of the MWC is divided into three parts to demonstrate its input and output dependence step by step. Part 1 includes a mixer that mixes the input signal with a mixing function $p_i(t)$ and an LPF that retains the mixed signal's baseband part. Part 2 indicates the conversion of the analog signal to the digital signal, while Part 3 shows digital processing such as digital modulations, support detection and reconstruction of the original signal. The design parameter notations are summarized in Table 2.1.

A periodic sign function (PSF) $p_i(t)$ is a periodically constant sequence with M length that switches the level between -1 and $+1$ for $T_p = 1/f_p$ interval. Formally,

$$p_i(t) = \alpha_{i,j}, \quad j\frac{T_p}{M} \le t \le (j+1)\frac{T_p}{M}, \quad 0 \le j \le M-1 \tag{2.3}$$

with a random $\alpha_{i,j} \in \{+1, -1\}$ [7]. A frequency-domain illustration of a PSF $p_i(t)$ that is decomposed into Fourier series coefficients $c_{i,l}$ located at lf_p is shown in Fig. 2.3(a). These

Table 2.1: MWC design parameters.

Design Parameters	Notation
Periodic Sign Function (PSF) frequency	f_p
Number of active bands	N
Number of slots in band of interest	L
Band of interest	$W = Lf_p$
Bandwidth of active band	B
Number of symbols in PSF	M
Number of channels	m
Carrier Frequencies	f_i
Number of digital channels in a single channel	q
Sampling rate of ADC	$f_s = qf_p$
Number of bits on ADC	NOB
Chipping frequency of PSF	$f_c = Mf_p$

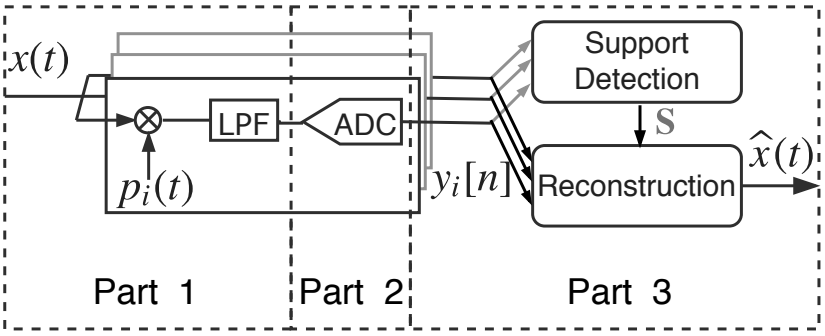

(a)

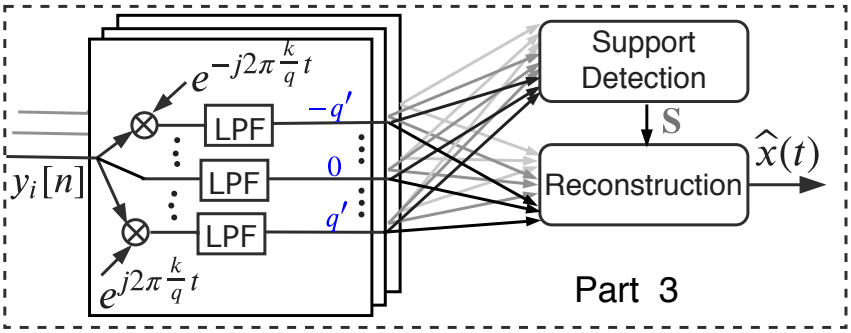

(b)

Figure 2.2: (a) Basic MWC system block diagram and (b) advanced MWC system back-end block diagram.

components downconvert corresponding bands or spectrum slices of the input signal with individual amplitudes as in Fig. 2.3(b). From Fig. 2.3(b), i-th digital output signal $y_i[n]$

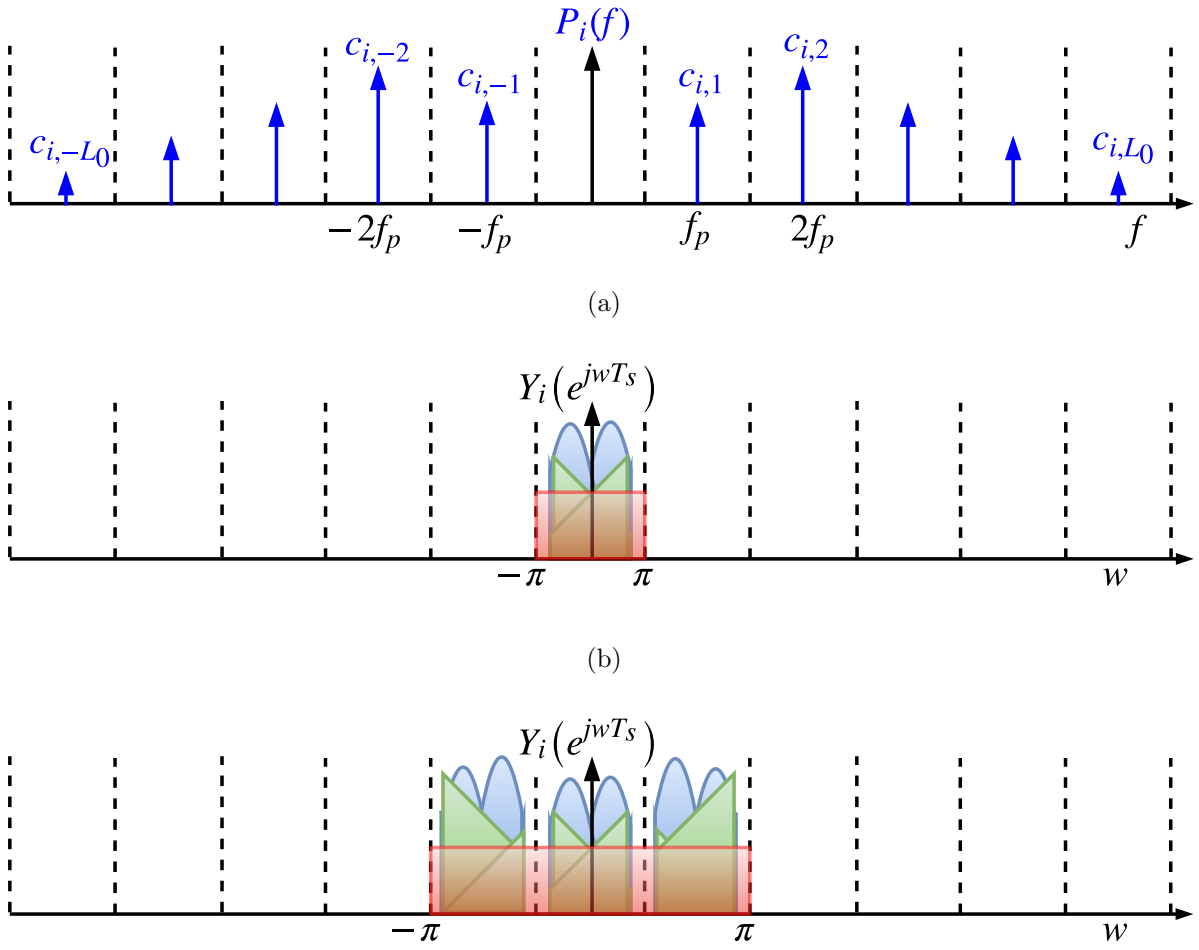

Figure 2.3: (a) Fourier series of the i-th PSF, (b) DTFT of the i-th sampled signal of basic MWC, (c) DTFT of the i-th sampled signal of advanced MWC.

through Fourier transform can be expressed as

$$Y_i(e^{jwT_s}) = \sum_{l=-L_0}^{L_0} c_{i,-l} Z_l(f). \tag{2.4}$$

In the case of the advanced MWC, q (> 1) digital channels are extracted from a single analog channel as shown in Fig. 2.2(b). For symmetry purpose, in the spectrum of sampled signal in Fig. 2.3(c), q must be odd such that $q = 2q' + 1$ where q' is an integer. Thus the

general form of (2.4) for the advanced MWC can be rewritten as

$$\acute{Y}_i(e^{jwT_s}) = \sum_{k=-q'}^{q'} \sum_{l=-L_0-k}^{L_0-k} c_{i,-(l+k)} Z_{l+k}(f - kf_p). \tag{2.5}$$

In other words, the parameter q of advanced MWC enables design flexibility between the number of analog channels and the complexity of digital signal processing.

If (2.4) is written as a vector signal $\mathbf{Y} = [Y_1(e^{jwT_s}), Y_2(e^{jwT_s}), ...Y_m(e^{jwT_s})]^T$ in matrix form, the generalized form can be expressed as

$$\mathbf{Y} = \mathbf{AZ}, \tag{2.6}$$

where $\mathbf{Z}$ points out separate spectrum slices of the input discrete-time signal and $\mathbf{A}$ is a sensing matrix that is defined only by Fourier series coefficients of all PSF signals as

$$[\mathbf{A}]_{i,j} = c_{i,j}, \quad i \in [1, m], \quad j \in [-L_0, L_0]. \tag{2.7}$$

For the advanced MWC, vector form of sampled signal $\mathbf{Y}$ can be achieved by collapsing each analog signal $\tilde{Y}_i(e^{jwT_s})$ into q digital channels using digital filter and mixers as shown in Fig. 2.2(b). Thus $\mathbf{Y} = [Y_1(e^{jwT_s}), Y_2(e^{jwT_s}), ...Y_{mq}(e^{jwT_s})]^T$ is obtained and (2.6) is the same for the advanced MWC by arranging sensing matrix as

$$[\mathbf{A}]_{i',j} = c_{i,j+k},\ i \in [1, m],\ k \in [-q', q'],\ j \in [-L_0, L_0] \tag{2.8}$$

where $i' = (i-1)q + k + q' + 1$. Once we have a digital vector signal, we have to recover support frequencies of active bands in the input wideband sparse signal using Greedy algorithms such as matching pursuit (MP), orthogonal matching pursuit (OMP), etc [16]. Recovered support frequency indicates nonzero signal indices of $\mathbf{Z} = [Z_{-L_0}(f), ..., Z_0(f), ..., Z_{L_0}(f)]^T$. These nonzero signals can be reconstructed using least-squares through the multiplication of the pseudo-inverse matrix as follows:

$$\hat{\mathbf{Z}}_{\mathbf{S}} = \mathbf{A}_{\mathbf{S}}^{\dagger}\mathbf{Y} \quad \text{s.t.} \quad \mathbf{S} = \text{supp}(\mathbf{Z}) = \{i : Z_i(f) \neq 0\}. \tag{2.9}$$

Here, subscript $\mathbf{S}$ denotes a set of row indices where $\mathbf{Z}$ takes nonzero values. In more detail, $\mathbf{A}_{\mathbf{S}}^{\dagger} = (\mathbf{A}_{\mathbf{S}}^{\mathbf{H}}\mathbf{A}_{\mathbf{S}})^{-1}\mathbf{A}_{\mathbf{S}}^{\mathbf{H}}$ and $\mathbf{A}_{\mathbf{S}}$ denotes a submatrix of $\mathbf{A}$ formed from column sets $\mathbf{S}$.

Theoretically, a necessary condition for perfect reconstruction is defined as follows: the number of channels m is needed to be $m \geq 2N$ for blind detection of arbitrary support frequencies of the input wideband sparse signal. In other words, the number of rows of $\mathbf{A}$ must be at least two times larger than the number of nonzero rows within $\mathbf{Z}$ [7], because an active band may occupy two spectrum slices. In this thesis, the carrier frequency is assumed to be an arbitrary frequency within a range $[0, L_0 f_p]$. These frequencies may lie at a boundary of two spectrum slots. Therefore, an active band can occupy up to two spectrum slices so that necessary condition can be determined as $m \geq 2N$. Once support frequencies are detected by Greedy algorithms from the input signal, active bands will be reconstructed through (2.9). To have a unique solution, the number of rows m in $\mathbf{A}$ must be equal to or larger than the number of rows or unknown $2N$ in $\mathbf{Z}$.

2.1.3 Support Recovery

The problem falls under solving sparse solutions of underdetermined linear systems. The famous works by Donoho [17] and Cand‘s et al. [18] firstly introduced the *compressed sensing* (CS), an emerging field. Mathematically, consider the linear system is given by

$$\mathbf{y} = \mathbf{A}\mathbf{z} \tag{2.10}$$

where the $m \times L$ matrix C has a nontrivial null space when $m < L$ as shown in Fig. 2.4(a). The goal of CS is to find a sparsest $\mathbf{z}$ vector among these solutions, in other words, a vector $\mathbf{z}$ has only a few nonzero entries. The unique sparse solution can be found via the

minimization program

$$\min_{z} \|\mathbf{z}\|_0 \qquad \text{s.t.} \qquad \mathbf{y} = \mathbf{A}\mathbf{z} \tag{2.11}$$

where $\|\mathbf{z}\|_0$ is the support of $\mathbf{z}$ which counts nonzeros in $\mathbf{z}$. Unfortunately, (2.11) program is NP-hard with combinatorial search. However, in practical, convex program is enough when number of nonzeros is sufficiently small which can be written as

$$\min_{z} \|\mathbf{z}\|_1 \qquad \text{s.t.} \qquad \mathbf{y} = \mathbf{A}\mathbf{z} \tag{2.12}$$

where $\|\mathbf{z}\|_1$ indicates sums of all entries of the vector $\mathbf{z}$. Another approaches for recovering sparse solution are greedy algorithms, which iteratively finds nonzero indices. For instance, *orthogonal matching pursuit* (OMP) [16] as described in Fig. 2.4(b). A residual vector $\mathbf{r}$ contains the part of $\mathbf{y}$ that is not spanned by the currently recovered indexed column. In OMP, an orthogonal projection $\mathbf{P_S y}$ is calculated in every iteration. The loop repeats until the index set S reaches a predefined limit or residual vector is sufficiently small. Once the algorithm terminated, the nonzero values $\mathbf{z_S}$ are computed by pseudoinversion of the corresponding columns of $\mathbf{A}$ matrix

$$\mathbf{z}_S[n] = \mathbf{A}_\mathbf{S}^\dagger \mathbf{y}[n] = (\mathbf{A}_\mathbf{S}^\mathbf{T}\mathbf{A}_\mathbf{S})^{-\mathbf{1}}\mathbf{A}_\mathbf{S}^\mathbf{T}\mathbf{y}[n] \tag{2.13}$$

Here, $\mathbf{z}[n] = [z_1[n], ..., z_L[n]]^T$ and $z_i[n]$ is the inverse-DTFT of $z_i(f)$ [6]. A complete reconstruction formula will be found at next subsection.

2.2 Trading Channels for Sampling Rate

The hardware cost, area and power are directly related to the total number of hardware devices, such as the mixers, the low-pass filters and the ADCs. It would be advantageous to reduce the number of devices as low as possible by increasing each ADC's sampling rate. Suppose $f_s = qf_p$ with odd $q = 2q' + 1$. Then the DTFT of the sample sequence

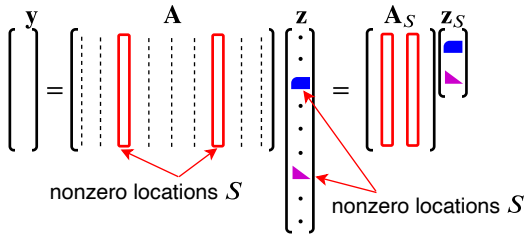

(a)

Orthogonal Matching Pursuit (OMP)

1. Initialization
$$S = \{\}, r \leftarrow \mathbf{y}$$
2. Find the most correlated column of $\mathbf{A}$ with r
$$\hat{i} = \text{argmax}_i \langle r, \mathbf{A}_i \rangle$$
3. Store the index into S
$$S \leftarrow S \cup \hat{i}$$
4. Calculate residue by substructing orthogonal projection
$$r \leftarrow \mathbf{y} - \mathbf{P}_S \mathbf{y}$$
5. Until (the predefined number of nonzeros is found) or (r is sufficiently small) Loop to 2

(b)

Figure 2.4: (a) An underdetermined system with a sparse solution vector. (b) Example sparse recovery OMP algorithm.

can be expressed as

$$y_i(f + kf_p) = \sum_{l=-L_0}^{+L_0} c_{i,(l+k)} X(f - lf_p) \tag{2.14}$$

where $-q' \leqslant k \leqslant q'$. Now we have q number of digital channels in each physical channel. However, additional digital computation is required to compute sample sequences from the spectrum of digitally q channels in each physical channel. Simple digital modulation and digital filter can separate these q channels from each physical channel's sampled sequence.

2.3 Reconstruction of the Original Signal

Actually, (2.6) is continuous in frequency, an infinite measurement vectors (IMV) problem. IMV conceptually requires infinite independent systems to solve a sparse solution of $\mathbf{z}(f)$. To avoid this difficulty of IMV, Mishali and Eldar proposed a continuous-to-finite (CTF) block in [8,19] recover the frequency support from the finite-dimensional system based on multiple measurement vector (MMV). The CTF block is the core of the MWC to detect frequency support without any prior information. The procedure is shown in Fig. 2.5. $\mathbf{z}(f)$ having a common nonzeros location set S over frequency. To take advantage of this

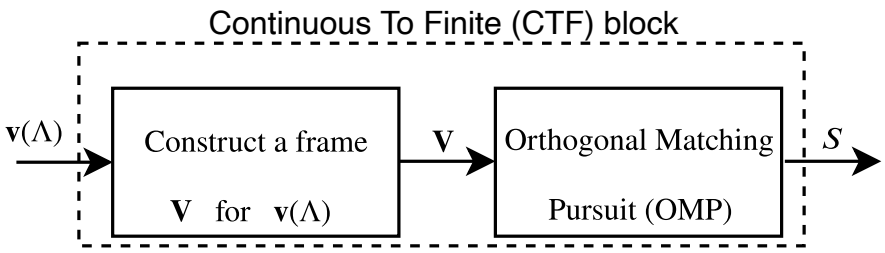

Figure 2.5: Recovery of the joint support $S = \text{supp}(\mathbf{z}(f))$.

joint sparsity, the CTF builds a basis from the measurements in time using 2.15

$$\mathbf{Q} = \int_{f \in \mathcal{F}_s} \mathbf{y}(f)\mathbf{y}^H(f)df = \sum_{-\infty}^{\infty} \mathbf{y}[n]\mathbf{y}^T[n] \tag{2.15}$$

where $\mathbf{y}[n] = [y_1[n], ..., y_m[n]]^T$ is the vector of samples at a time nT_s. Then, there is exits $\mathbf{V}$ frame matrix of $\mathbf{y}(f)$ such that $\mathbf{Q} = \mathbf{V}\mathbf{V}^H$ [19].

Once support is found from CTF block, waveform reconstruction formula can be written as

$$x[n] = x(nT) = \sum_{i \in S} (\tilde{z}_i[n] * h_I[n]) e^{2\pi i f_p nT} \tag{2.16}$$

Here, $\tilde{z}_i[n]$ is interpolated version of $\mathbf{z}[n]$ from (2.13).

First necessary condition for the perfect reconstruction comes from aliasing-effect on the each ADC that is $f_s \geqslant f_p$. Second necessary condition $m \geqslant 2N$ allows to have enough linearly independent equations in (2.6).

2.4 Sensing Matrix Generation

Sensing matrix $\mathbf{A}$ in (2.6) is one of the most important characteristics of the MWC system. Depending on the selection of the sensing matrix, whole system performance depends on it. In order to measure robustness of the sensing matrix in compressed sensing field, authors of [20] introduced *Restricted Isometry Property*(RIP).

$$(1 - \delta_k)||x||_2^2 \leqslant ||Ax||_2^2 \leqslant (1 + \delta_k)||x||_2^2 \tag{2.17}$$

for all $x \in \sum_k$. If a matrix $\mathbf{A}$ satisfies 2.17 the RIP of order $2k$, then it says that $\mathbf{A}$ approximately preserves the distance between any pair of k-sparse vectors. Unfortunately, computing RIP constants δ_k is NP-hard. For that reason, matrix coherence is used practically instead of RIP [21]. The coherence of $\mathbf{A}$, denoted $\mu(\mathbf{A})$, is the largest inner product between any two columns $\mathbf{a}_i$,$\mathbf{a}_j$ of $\mathbf{A}$:

$$\mu(\mathbf{A}) = \max_{1 \leqslant i \leqslant j \leqslant n} \frac{|\langle \mathbf{a}_i, \mathbf{a}_j \rangle|}{||\mathbf{a}_i||_2 ||\mathbf{a}_j||_2} \tag{2.18}$$

The achievable lower bound is known as the *Welch bound* [22] by $\sqrt{\frac{n-m}{m(n-1)}} \leqslant \mu(\mathbf{A}) \leqslant 1$.

2.5 Compressibility of Signals

Generally, input wideband signal can be sparse in any transform or any space, not necessarily on frequency domain. Compression loss happens if signal is not perfectly sparse in the chosen domain. In order to quantify the loss, we will use following formula for measuring compression loss

$$\sigma_k(x) = \min_{\hat{x} \in \sum_k} ||x - \hat{x}|| \tag{2.19}$$

Here, $\sum_k$ is a set of k-sparse signals. In our case, $\sigma(x)$ will be the power of other sideband spectrum slices, and $\sum_k$ will be a clean bandpass signal that lies in only one band.

2.6 Comparison with Other Sub-Nyquist Samplers

Compared to other sub-Nyquist, samplers including periodic nonuniform sampler with time-interleaved ADCs [23], the MWC has several advantages such that a precise multiphase clock is no longer needed and that carrier frequencies are unnecessary to be known in advance. In addition, a remarkable asset is design flexibility that allows trade-off choice between each ADC sampling rate and the number of channels. Two common architectures of the MWC exist in previous researches. The first architecture is defined as a *direct MWC* that directly converts the input signal without any down-converter. It is also known as

low-pass compressed sensing (CS) architectures that senses a frequency range from DC to f_{max} as demonstrated in [6–10],adams2017. Second architecture is defined as an *indirect MWC*, which is also called as quadrature analog-to-information converter (QAIC) or time-segmented QAIC (TS-QAIC) as introduced in [24–26]. It converts the input signal using a downconverter in front of the MWC and senses the spectrum from f_{min} to f_{max}. There is also similar sub-Nyquist sampler architecture, which is called *random demodulator*, that is the same as a single channel of the MWC [27–29].

2.7 Current Challenges in the MWC Implementation

To the best of our knowledge, some practical challenges will be explained in this section. The first practical challenge we have noticed is that, when we reconstruct some wideband sparse signal based on the MWC, there was some increment on the noise floor as shown in Fig. 2.6. Moreover, this NF degradation was not formally analyzed before.

In [9], the prototype circuit for MWC was designed to have 15 dB SNDR, which they defined is a sufficient level for successful detection of carrier frequencies from the input sparse wideband signal with subsequent digital processing under necessary condition. The total NF analysis of the system was made until the output of the ADC. In some advanced applications, such as high-precision test measurement for sparse wideband signals, much higher target SNDR would be required.

In [10] and [11], the prototype MWC system was designed for signal detection and blocker rejection simultaneously. The important idea for noise analysis was the noise-folding gain in the mixer of MWC. When the mixer aliases the whole wideband signal into the baseband, the noise floor will also be folded and accumulated. They also pointed out that this folding gain can be estimated by a ratio of the gain of a Fourier series coefficient that corresponds to the carrier frequency in the mixing function and the sum of all the coefficients' gains within the band of interest. In reality, when reconstructing the original wideband signal, matrix operation has to be performed to multiply a pseudo-inverse of reduced sensing matrix, which includes columns indexed by indices of recovered nonzero

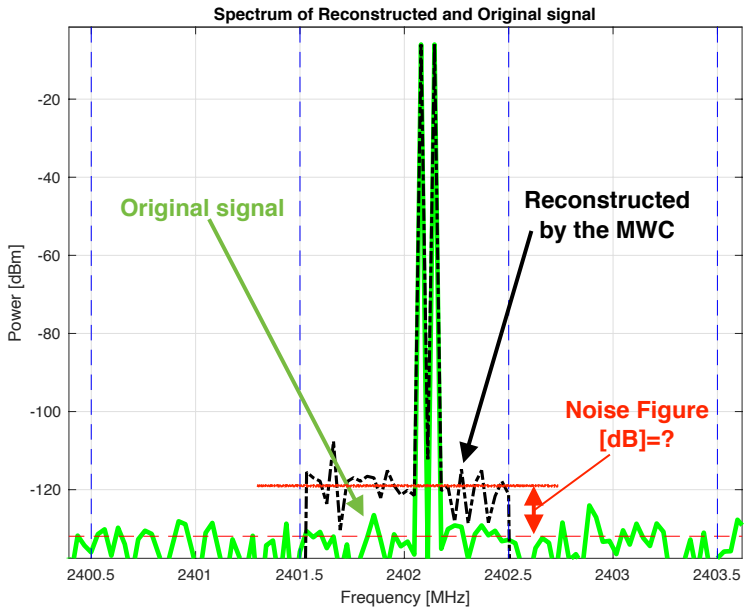

Figure 2.6: Noise figure of the MWC.

elements with received vector signal. This operation also affects noise performance even though it is done in the digital domain.

To use the MWC in a practical RF receiver, we need to estimate the NF of MWC to optimize the sensitivity of the receiver.

The subsequent challenges are all related to each other. There are several factors that affect the sensing matrix. Without calibration of the sensing matrix, we will have unwanted spurs or images in the reconstructed spectrum. The first non-ideal thing in practical implementation is the waveform shape of the PSF as shown in Fig. 2.7. Here we have the ideal PSF as in dashed black. The blue lines are actual PSF, which is directly measured by a real-time oscilloscope. That means the coefficients of the sensing matrix will be changed. Also, there is timing mismatch and gain mismatch on the PSFs along different channels due to non-ideal hardware components. These mismatches will also introduce some unwanted deviation on the sensing matrix.

Another factor is the time difference between PSF and the ADC clock, as illustrated in Fig. 2.8. Initially, this time offset does not exist in an ideal situation. Nevertheless, in

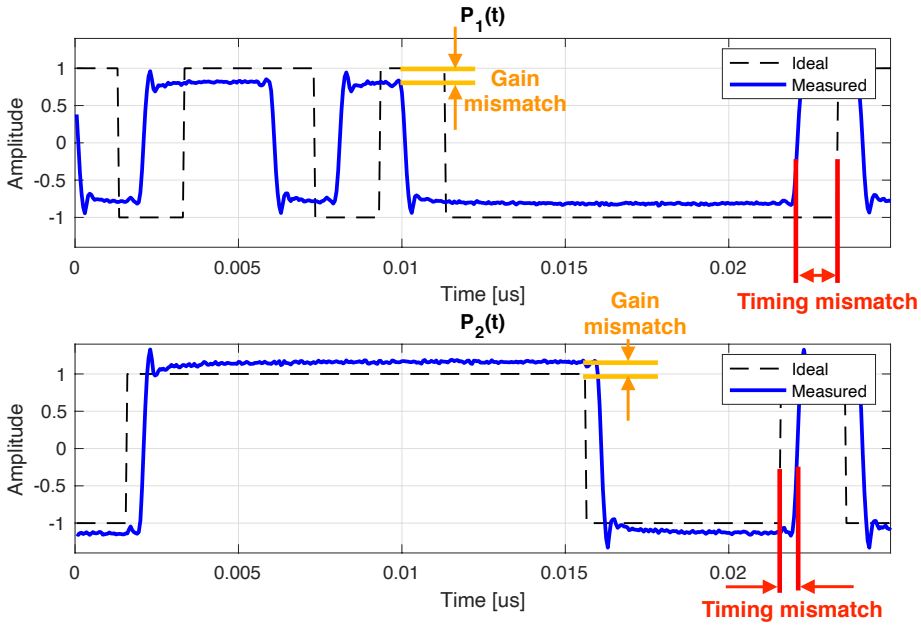

Figure 2.7: Mismatches of the PSF.

the practical implementation, we will have some time offset between PSF and ADC clock due to some delays of cables. This unwanted offset will introduce some phase shifts on the sensing matrix.

Depending on the input bandwidth of the mixer, we have a non-flat frequency response in the mixer as depicted in Fig. 2.9. This non-flatness will also affect the sensing matrix.

Lastly, there is still some unwanted gains on the stopband of the non-ideal LPF, as shown in Fig. 2.10. This non-ideality will allow some unwanted components to pass

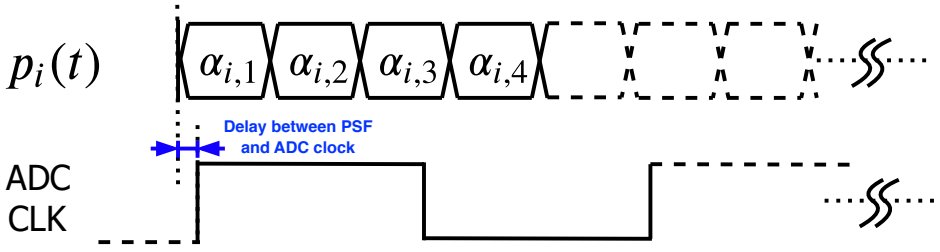

Figure 2.8: Delay between PSF and ADC clock.

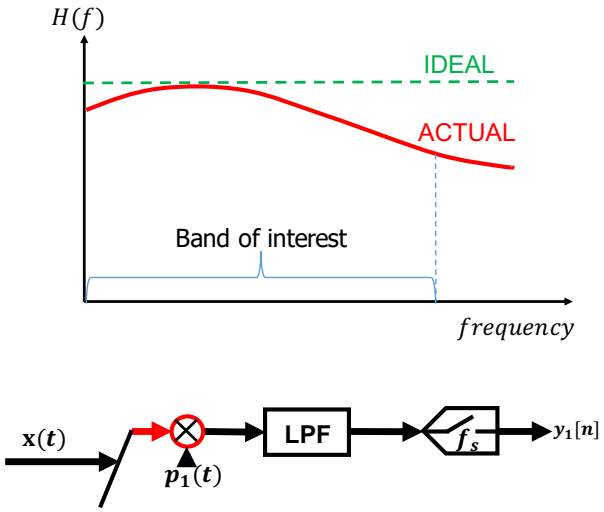

Figure 2.9: Non-ideal frequency response of the input signal path.

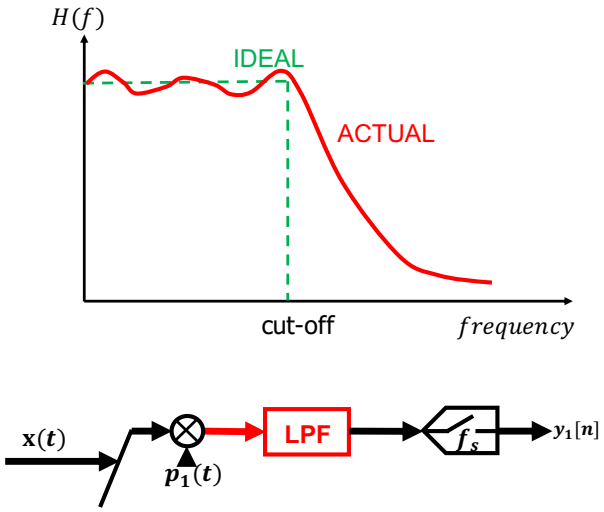

Figure 2.10: Non-ideal frequency response of the analog low-pass filter.

through the filter. That also affects the sensing matrix. All of them should be taken into account when we realize the MWC system. Without the calibration of the sensing matrix, the reconstruction performance is extremely limited.

Chapter 3

Simulations on MWC Reconstruction of Various Signals and Jitter Impacts

This chapter introduces the MATLAB simulation model of MWC and its performance analysis on selecting various design parameters and periodic sign functions (PSF). The simulation model has shown in Fig. 3.1.

3.1 MWC Design Parameters

Selection of design parameters of MWC for the specific application of Bluetooth signal waveform generation shown in Table 3.1.

To quantify the similarity between the reconstructed waveform and original waveform, Normalized Mean Square Error (NMSE) (3.1) is used for the simulation. The unit is [dB].

$$NMSE_{dB} = 20\log_{10}\left(\frac{||x_w(t) - \hat{x}_w(t)||}{||x_w(t)||}\right) \tag{3.1}$$

where $x_w(t), \hat{x}_w(t)$ correspond to windowed original signal and windowed reconstructed signal. Blackman windowing function was used on this measurement for reducing DFT

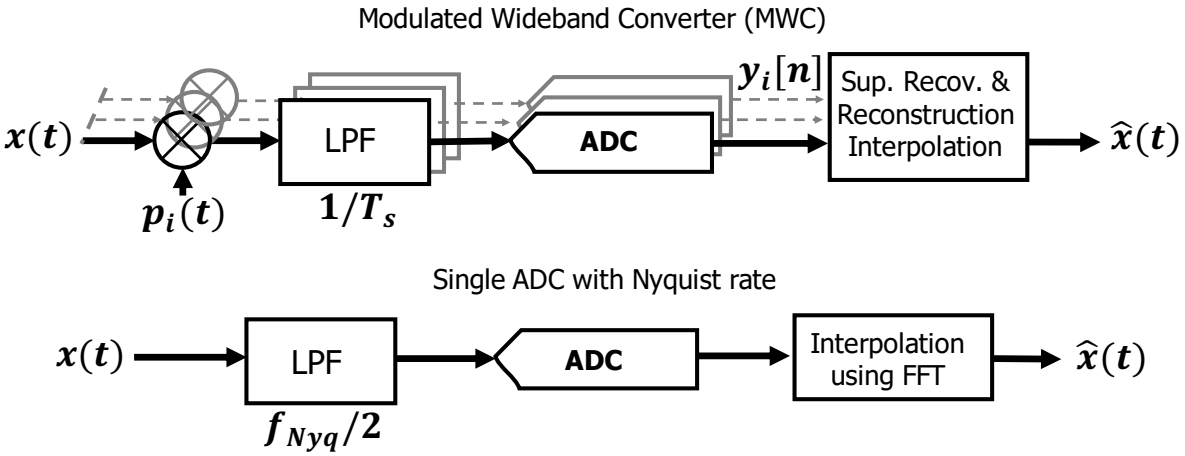

Figure 3.1: Simulation model of MWC based on MATLAB

Table 3.1: MWC configuration

Parameter	Value	Description
f_{nyq}	161 MHz	Nyquist rate
B	1 MHz	Bluetooth Bandwidth
f_p	1 MHz	Frequency for PSF
q	1	# of digital channels
f_s	f_p	Sampling rate on each ADC
L	161	Aliasing rate
M	L	# of symbols in a period of PSF

artificial distortion.

3.2 MWC Reconstructions on Sparse Signals

First, two kinds of input signals are used as an input of MWC. To check performance for a clean sparse signal, we created a low-crest multi-tone signal with equally frequency spaced in one band. A Bluetooth sparse signal (not the perfectly sparse case) is created for more practical applications.

a. Passband Low-crest Multi-tones Signal Generation

Multi-tones signals are useful signals for measuring characteristics of a linear system [30], for example, the impulse response or the frequency response of a filter or communication channel. The frequencies of the multi-tones should be carefully chosen based on the frequency resolution of the measurement. If the frequency is not aligned to the FFT bins, the spectrum presents undesirable components as shown in Fig. 3.2(a). On the other hand, if the frequencies are correctly aligned to the FFT bins, the spectrum can achieve clean multi-tones without any spurs as shown in Fig. 3.2(b).

In practice, most systems are peak-power limited and the measurement is always contaminated by additive noise. Therefore, in order to maximize Signal-to-Noise Ratio (SNR), it is desirable to have a low-crest factor of the signal. The Crest Factor (CF) formula of the complex multi-tones signal $m(t)$ is defined by

$$\mathrm{CF} = \max_{t\in[0,T]}\{|m(t)|\} \Big/ \sqrt{\frac{1}{T}\int_0^T |m(t)|^2 dt} \tag{3.2}$$

Note that the CF of a multi-tones signal with a single tone is $CF = 1$ in the complex case and $CF = \sqrt{2}$ in the real-valued case. In multi-tones case, minimum peak voltage can be obtainable at optimum phases to achieve minimum CF.

There are several methods for the generation of the low-crest multi-tones signal. If tones are equally-spaced with each other, analytic optimum solution for phases was found

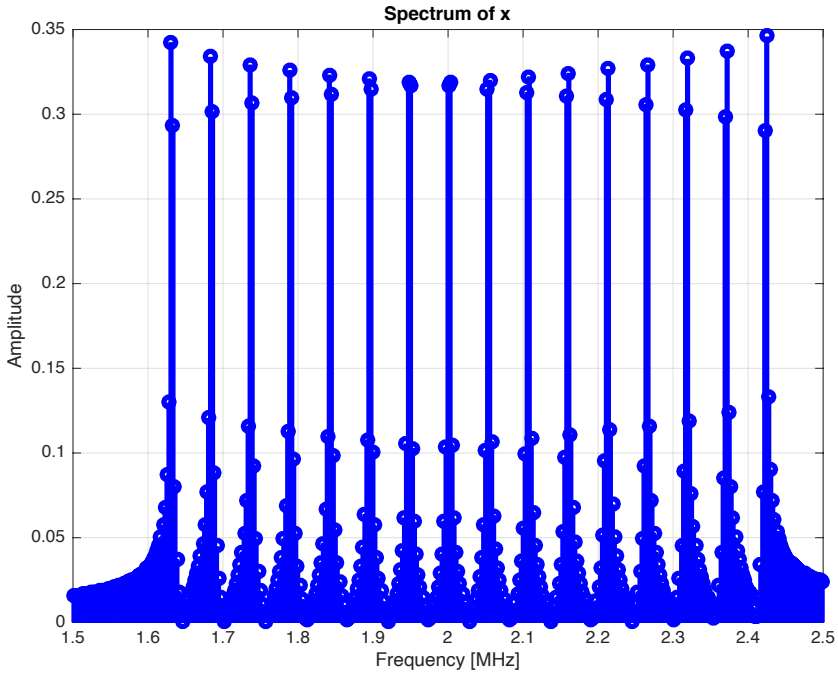

(a)

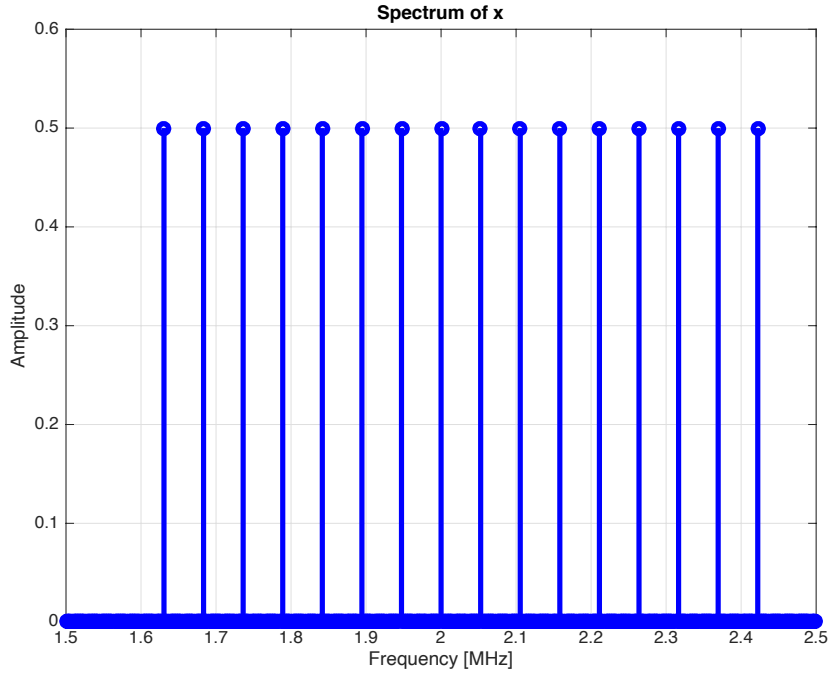

(b)

Figure 3.2: Frequency-domain spectrum of the multi-tones with the unaligned frequencies to the FFT bins (a), and frequency-domain spectrum of the multi-tones with the aligned frequencies to the FFT bins (b).

on [31]. Generally, iterative algorithms are proposed for finding the global optimum point of phases in [32]. Among these algorithms, Fourier transform-based method shows the lowest CF for arbitrary frequency tones. In this simulation, we used 16 multi-tones signals that all tones lie within 1 MHz with equally spaced depicted in Fig. 3.2b. The phases of the multi-tones were all zeros in the first simulation. In this case, the CF was not satisfactory as shown in the Fig. 3.3(a). If the phases of the multi-tones are determined by Newman's phases [32], the CF is dramatically decreased as shown in Fig. 3.3(b).

The time-domain waveform of the reconstructed multi-tones is shown in Fig. 3.4(a). At the same time, the spectrum reconstructed multi-tones by the MWC is shown in Fig. 3.4(b). When the input signal is a low-crest Multi-tone signal, NMSE shows near -100 dB between reconstructed and original waveform. It means the MWC system almost makes the perfect recovery with the total sampling rate 8 MHz ($m = 8$ channels, $f_s = 1MHz$ each sampling rate for ADC) in the boundary of the necessary condition.

3.3 MWC Reconstructions on Bluetooth 1.0 Signal

This chapter is removed in this abridged version.

3.4 MWC Reconstructions on Bluetooth 2.0 Enhanced Data Rate (EDR) Signal

This section is removed in this abridged version.

3.5 Jitter Impact in the MWC

This section is removed in this abridged version.

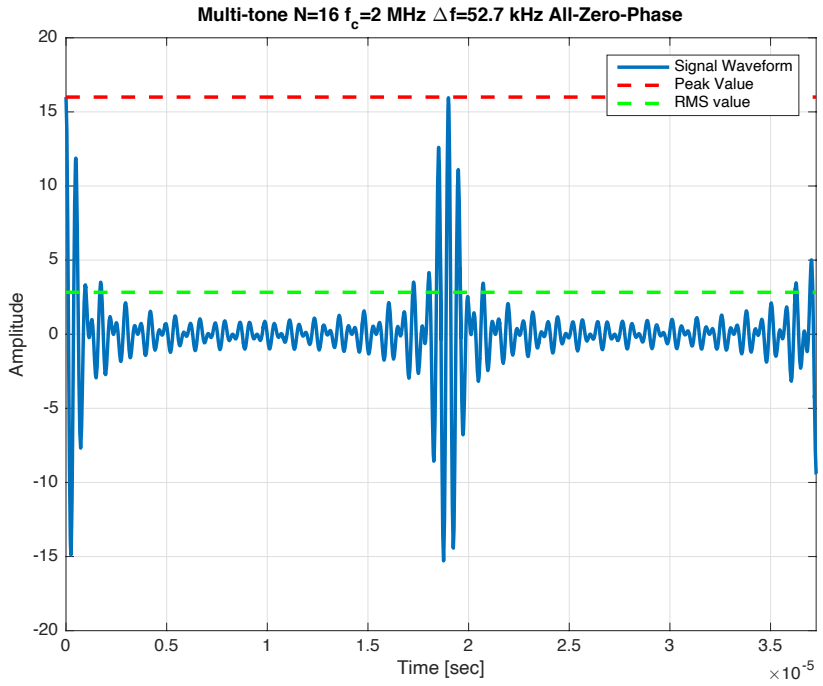

(a)

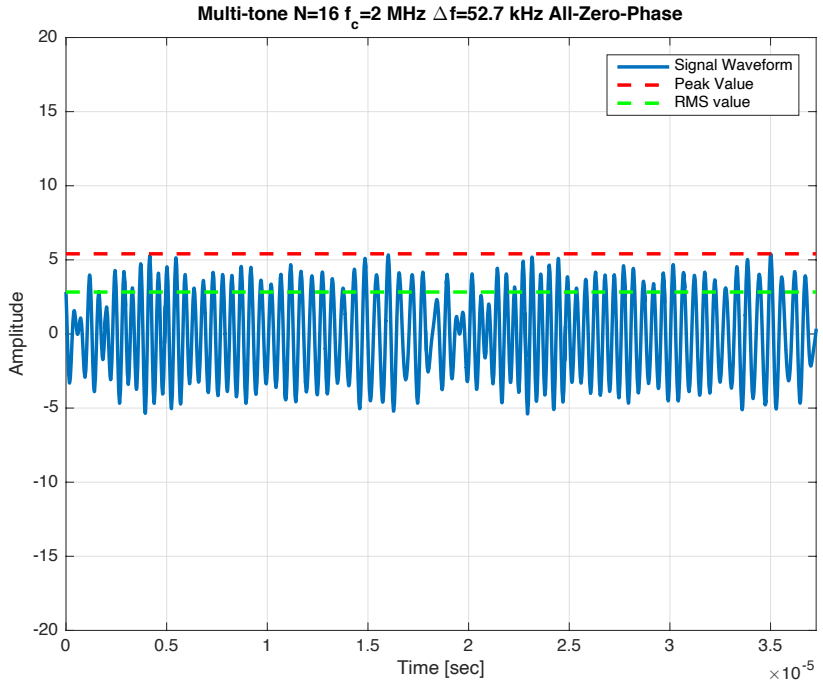

(b)

Figure 3.3: Time-domain waveform of the multi-tones with zero phases (a), and time-domain waveform of the multi-tones with Newman's phases (b).

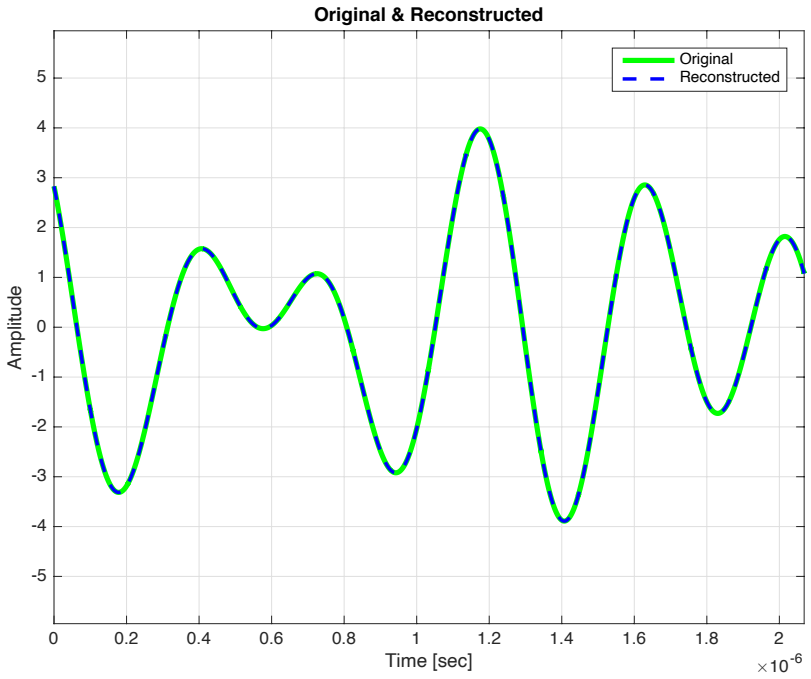

(a)

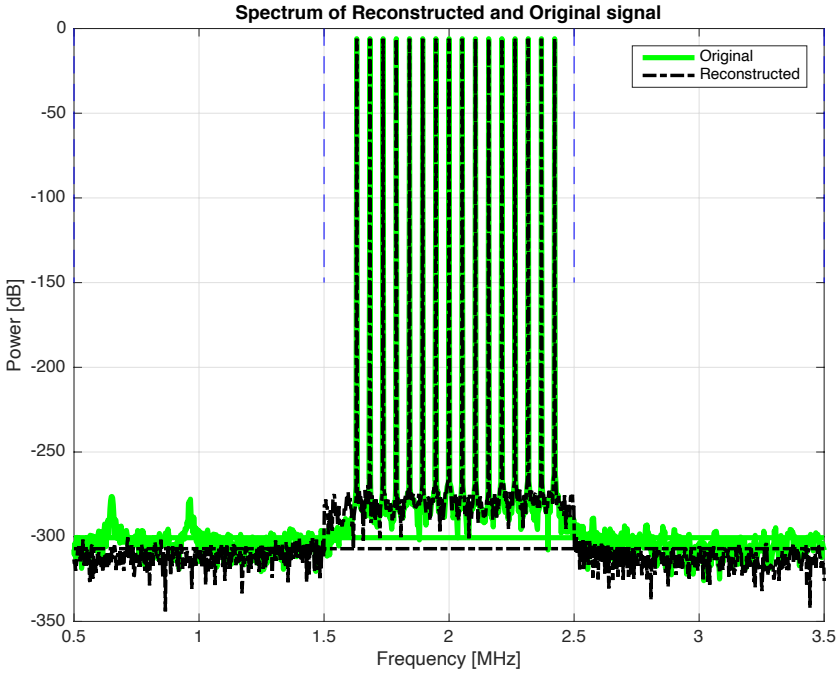

(b)

Figure 3.4: Time-domain waveform of the reconstructed multi-tones (a), and frequency-domain spectrum of the reconstructed multi-tones (b).

3.6 Summary

Also, perfect recovery conditions are well-defined. However, non-ideal hardware components always introduce some undesirable situations in a practical case. First, non-ideal mixing function as described in Fig. 2.2(a) causes several issues. According to the orthogonality of the matrix in the (2.6), it determines the main ability to recover each spectrum portion $\mathbf{z}$ in (2.6). As long as we have a high rank of the matrix and a low mutual coherence of the matrix, perfect recovery of the support and recovery of the original signal is guaranteed. Another issue of the non-ideal mixing function is transitioning between signs in the time domain. High-frequency components of the mixing function Fourier series will be significantly reduced; it limits the input signal bandwidth. Second, the non-ideal low-pass filter in Fig. 2.2(a) presents some unwanted frequency component to the output due to the transition bands around the cut-off frequency. These unwanted components will be aliased into the converted digital signal during sampling and impossible to remove. Another non-ideal filter issue can be compensated in the digital domain, which is a non-flatness of the transfer function. Once the shape is measured, an equalization filter can easily suppress the effect caused by non-flatness. The third issue is related to the optimization of design parameters.

Chapter 4

Comprehensive Analytical Definition of the Noise Figure on MWC and its Validation in Simulation

4.1 Noise Figure of the MWC

In this chapter, the noise performance of MWC is investigated then its noise figure is defined analytically. The thermal noise, which has a uniform distribution in the frequency domain, is assumed as the input-referred noise to simplify the calculation of the whole system's noise performance. Noise factor F of any systems is defined as [33]

$$\mathrm{F} = \frac{SNR_{\mathrm{IN}}}{SNR_{\mathrm{OUT}}}. \tag{4.1}$$

Noise figure NF is a decibel form of the noise factor as given by

$$\mathrm{NF} = 10\log_{10}(\mathrm{F}) = SNR_{\mathrm{IN,\ dB}} - SNR_{\mathrm{OUT,\ dB}}, \tag{4.2}$$

where SNR_{out} is a power ratio of the output signal and noise that is defined within the total effective bandwidth of NB. Since the reconstruction process recovers only N active

bands that are defined by $\mathbf{S}$ in (2.9), SNR_{in} is also defined by a power ratio of signal and input-referred noise within the total effective bandwidth of the active bands NB as in the case for SNR_{out}. The noisy sparse signal within the band of interest can be modeled as

$$\tilde{X}(f) = \underbrace{\sum_{l\in\mathbf{S}} Z_l(f - lf_p)}_{\text{signal term as } X(f) \text{ in (2.2)}} + \underbrace{\sum_{l=-L_0}^{L_0} W_l(f - lf_p)}_{\text{noise term}}, \tag{4.3}$$

where $W_l(f)$ is a spectrum slice of the thermal noise as shown in Fig. 2.1. These Fourier transforms are assumed to be bandlimited baseband signal $Z_l(f) = 0, |f| > f_p/2$. Let us assume that the average signal power in each active band is defined as

$$P_l = \int_{-f_p/2}^{f_p/2} \|Z_l(f)\|^2 \, df \quad \text{where} \;\; l \in \mathbf{S} \tag{4.4}$$

and the total power is expressed as

$$NP_s = \sum_{l\in\mathbf{S}} P_l \quad \text{where} \;\; l \in \mathbf{S}. \tag{4.5}$$

For the thermal noise, the average powers of each spectrum slice are expected to be

$$P_n = \int_{-f_p/2}^{f_p/2} \|W_l(f)\|^2 \, df \qquad \text{for all} \;\; l. \tag{4.6}$$

Therefore, the input SNR is given by

$$SNR_{\text{IN}} = \frac{\int_{-\infty}^{\infty} \left\| \sum_{l \in \mathbf{S}} Z_l(f - l f_p) \right\|^2 df}{\int_{-\infty}^{\infty} \left\| \sum_{l \in \mathbf{S}} W_l(f - l f_p) \right\|^2 df} = \frac{\sum_{l \in \mathbf{S}} \int_{-f_p/2}^{f_p/2} \|Z_l(f)\|^2 df}{\sum_{l \in \mathbf{S}} \int_{-f_p/2}^{f_p/2} \|W_l(f)\|^2 df} = \frac{\sum_{l \in \mathbf{S}} P_l}{N P_n} = \frac{P_s}{P_n}. \tag{4.7}$$

Here spectrum slices $Z_l(f)$ are assumed to be disjoint with each other so it can be written as a sum of norms. Another way of stating (4.7) is to say

$$SNR_{\text{IN}} = \frac{P_s}{P_n} = \frac{\|\mathbf{Z_S}\|_{\mathbf{F}}^2}{\|\mathbf{W_S}\|_{\mathbf{F}}^2}, \tag{4.8}$$

where $\|\mathbf{X}\|_{\mathbf{F}}$ is a Frobenius norm of the $m \times n$ matrix $\mathbf{X}$ defined as

$$\|\mathbf{X}\|_{\mathbf{F}} = \left(\sum_{i=1}^{m} \sum_{j=1}^{n} |x_{i,j}|^2 \right)^{\frac{1}{2}}. \tag{4.9}$$

The matrix form (4.8) shows more practical definition rather than (4.7) because it is a discretized form. Substituting (4.3) into (2.6) yields

$$\mathbf{Y} = \mathbf{A}(\mathbf{Z} + \mathbf{W}), \tag{4.10}$$

where $\mathbf{W}$ is separate spectrum slices of discrete-time input-referred noise or discretized matrix form of the noise term in (4.3) similarly to $\mathbf{Z}$ in (2.6). Thus, the reconstructed signal (2.9) becomes

$$\hat{\mathbf{Z}}_{\mathbf{S}} = \mathbf{A}_{\mathbf{S}}^{\dagger}(\mathbf{AZ} + \mathbf{AW}). \tag{4.11}$$

Here, the impact of the input-referred noise at the reconstructed signal can be clearly seen.

4.1.1 Noise Factor of Mixer and LPF

First part of the basic MWC system consists of a mixer and an LPF as shown in Fig. 2.2(a). In this part, noise folding gain will be introduced in the mixer. The output signal of the LPF in i-th channel is given by

$$\tilde{Y}_i(f) = \sum_{l \in \mathbf{S}} c_{i,-l} Z_l(f) + \sum_{l=-L_0}^{L_0} c_{i,-l} W_l(f), \tag{4.12}$$

where the first term indicates a linear combination of signal that aliased into baseband as shown in Fig. 2.3(b), while the second term shows a linear combination of noise that are also aliased into baseband and accumulated as illustrated by red rectangle in Fig. 2.3(b). Through the multiplication with the PSF, at the output of the mixer the signal power spreads across kf_p frequencies for all integer k with the weight of $c_{i,k-l}$ for $Z_l(f)$. Then only the weighted copies at baseband are extracted with the LPF. On the other hand, the noise power, which is uniformly distributed throughout the original band of interest, is folded at baseband after the weighting. Then the output SNR of the mixer and LPF part is defined as

$$\begin{aligned} SNR_{i\text{-th MIXLPF}} &= \frac{\int_{-f_p/2}^{f_p/2} \left\| \sum_{l \in \mathbf{S}} c_{i,-l} Z_l(f) \right\|^2 df}{\int_{-f_p/2}^{f_p/2} \left\| \sum_{l=-L_0}^{L_0} c_{i,-l} W_l(f) \right\|^2 df} \\ &= \frac{\sum_{l \in \mathbf{S}} \int_{-f_p/2}^{f_p/2} \left\| c_{i,-l} Z_l(f) \right\|^2 df}{\sum_{l=-L_0}^{L_0} \int_{-f_p/2}^{f_p/2} \left\| c_{i,-l} W_l(f) \right\|^2 df}. \end{aligned} \tag{4.13}$$

Here, active band signals and noise spectrum slices are independent with each other. Thus,

$$\int W_i(f)W_j^*(f)df = 0 \text{ and} \tag{4.14}$$

$$\int Z_i(f)Z_j^*(f)df = 0, \tag{4.15}$$

for all $i \neq j$. Using this property, (4.13) is rewritten as

$$SNR_{i\text{-th MIXLPF}} = \frac{\sum_{l\in\mathbf{S}} \|c_{i,-l}\|^2 \int_{-f_p/2}^{f_p/2} \|Z_l(f)\|^2 df}{\sum_{l=-L_0}^{L_0} \|c_{i,-l}\|^2 \int_{-f_p/2}^{f_p/2} \|W_l(f)\|^2 df}. \tag{4.16}$$

Under an assumption that the power of noise spectrum slices are constant within the band, we substitute (4.4) and (4.6) into (4.16). Then we obtain

$$SNR_{i\text{-th MIXLPF}} = \frac{\sum_{l\in\mathbf{S}} \|c_{i,-l}\|^2 P_l}{\sum_{l=-L_0}^{L_0} \|c_{i,-l}\|^2 P_n}. \tag{4.17}$$

The noise gain or noise folding gain can be seen clearly on this equation. If we assume the average signal power of each active band P_l are constant over all l, noise factor (F) of the first part at the i-th channel is simplified to

$$\mathrm{F}_{i\text{-th MIXLPF}} = \frac{SNR_{\mathrm{IN}}}{SNR_{i\text{-th MIXLPF}}} = \frac{\sum_{l=-L_0}^{L_0} \|c_{i,-l}\|^2}{\sum_{l\in S} \|c_{i,-l}\|^2}. \tag{4.18}$$

4.1.2 Noise Factor of ADC

For the second part of Fig. 2.2(a), which has ADC only, the noise figure of this part is determined as

$$\mathrm{NF}_{i\text{-th ADC}} = SNR_{i\text{-th MIXLPF, dB}} - SNR_{i\text{-th ADC, dB}}, \tag{4.19}$$

where $SNR_{i\text{-th ADC, dB}}$ is the SNR at the output of the ADC in the i-th channel. $\mathrm{NF}_{i\text{-th ADC}}$ may increase due to the quantization noise of the ADC.

4.1.3 Noise Factor of the MWC System

In the last part of the basic MWC, reconstruction operation includes matrix multiplication and several modulations and additions in the digital domain as explained in Chapter 2. The only effective block on noise is matrix multiplication. So it is sufficient to define a noise factor on the output of reconstruction multiplication. Beforehand, we define the output SNR of the reconstruction including the operation of the mixer in the first part as

$$SNR_{\mathrm{OUT}} = \frac{\|\mathbf{Z_S}\|_{\mathbf{F}}^2}{\left\|\hat{\mathbf{Z}}_{\mathbf{S}} - \mathbf{Z_S}\right\|_{\mathbf{F}}^2} \tag{4.20}$$

where $\mathbf{Z_S}$ is a submatrix of $\mathbf{Z}$ in (2.6) with rows indicated by $\mathbf{S}$ which is a set of row indices where $\mathbf{Z}$ takes nonzero values as defined by (2.9), while $\hat{\mathbf{Z}}_{\mathbf{S}}$ specifies reconstructed version of $\mathbf{Z_S}$. By substituting (4.11) into the denominator of (4.20) under the assumption that we have the necessary condition for perfect reconstruction as discussed in Chapter 2, we have

$$SNR_{\mathrm{OUT}} = \frac{\|\mathbf{Z_S}\|_{\mathbf{F}}^2}{\left(\left\|\mathbf{A}_{\mathbf{S}}^{\dagger}\mathbf{AZ} + \mathbf{A}_{\mathbf{S}}^{\dagger}\mathbf{AW} - \mathbf{Z_S}\right\|_{\mathbf{F}}^2\right)} \tag{4.21}$$

$$= \frac{\|\mathbf{Z_S}\|_{\mathbf{F}}^2}{\left\|\mathbf{A}_{\mathbf{S}}^{\dagger}\mathbf{AW}\right\|_{\mathbf{F}}^2} = \frac{P_s}{\left\|\mathbf{A}_{\mathbf{S}}^{\dagger}\mathbf{A}\right\|_{\mathbf{F}}^2 P_n} \tag{4.22}$$

Combining (4.22), (4.8) and (4.1), the total noise factor of MWC on $\mathbf{S}(\xi)$, which is a ξ-th support out of all possible supports within $\binom{L/2}{N/2}$ slots in band of interest, can be written as

$$\mathrm{F}_{\mathrm{TOTAL}}(\xi) = \frac{SNR_{\mathrm{IN}}}{SNR_{\mathrm{OUT}}} = \left\| \mathbf{A}^{\dagger}_{\mathbf{S}(\xi)} \mathbf{A} \right\|^2_{\mathbf{F}}. \tag{4.23}$$

The total noise factor of MWC is expressed in decibel form as $\mathrm{NF}_{\mathrm{TOTAL}}(\xi) = 10\log_{10}(\mathrm{F}_{\mathrm{TOTAL}}(\xi))$. The NF of the prior part (4.17) is implicitly included in (4.23) as the rows of the term $\mathbf{A}$ carries the denominator part of (4.17), while elements of $\mathbf{A}^{\dagger}_{\mathbf{S}}$ contributes the noise factor of the reconstruction part.

4.1.4 Average Noise Figure (ANF)

The total NF of MWC strongly depends on the carrier frequency of the active band. Thus the choice of PSF and the location of the active bands within the band of interest are also very important to evaluate the total noise figure. For that reason, it is difficult to compare our analysis with currently implemented MWC systems based only on several measurement instances without knowing specific PSF waveforms. Therefore, in order to unify all these noise figures of the MWC that is designed by the same parameters, we introduce an average noise figure (ANF) that is defined by

$$\mathrm{ANF}_{\mathrm{TOTAL}} = 10\log_{10}\left(\frac{1}{L_0}\sum_{\xi=1}^{L_0}\mathrm{F}_{\mathrm{TOTAL}}(\xi)\right) \tag{4.24}$$

This ANF result shows only MWC's noise performance. In practice, RF front-end circuits will be used in front of MWC, which may dominate the total NF, as will be discussed in Sect. 4.2.3.

4.2 Simulation Results

In this section, the average NF defined in the previous section will be compared with MATLAB-based simulation results. The MATLAB code is implemented based on a

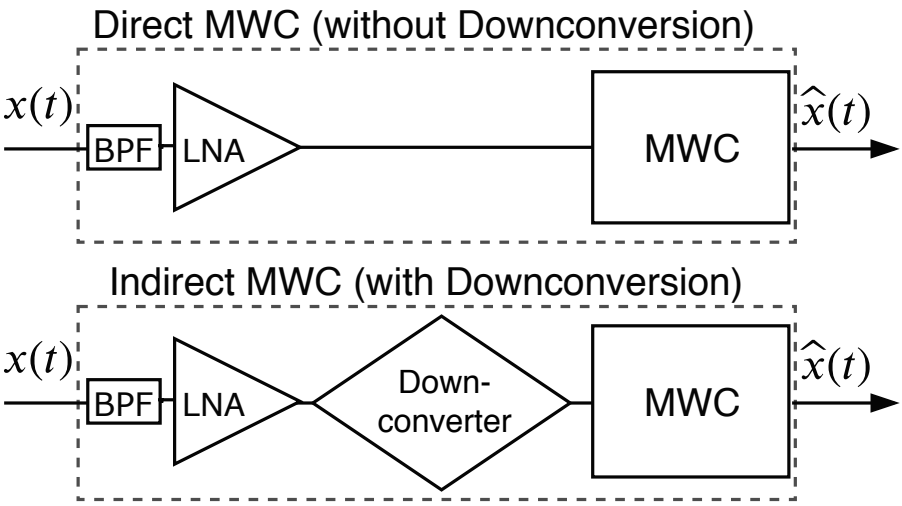

Figure 4.1: MWC-included architectures.

demonstration by M. Mishali and Y. C. Eldar [34]. We take into account the following assumption in this simulation for straightforward understanding.

- *Infinite precision ADC & Full-scale input on ADC:* For simplicity purpose, we set sufficiently large NOB on each ADC and set the peak-to-peak amplitude of the ADC input signal into full-scale of the ADC. This assumption makes the noise figure of the ADC 0 dB in Fig. 2.2(a).

4.2.1 Wideband Sparse Signal Generation

In this part, we will explain wideband sparse analog signal generation method. Prior MWC systems assume that the input signal exploits all carrier frequencies from DC to Nyquist frequency. But in practice, sparse wideband signal locates in specific bandpass region depending on the application. So, in the simulation part, we used the MWC system in two kinds of architectures for the passband sparse signal as depicted in Fig. 4.1. First architecture is the direct (w/o D.C.) MWC as presented in [6–11] that directly converts the wideband sparse signal after bandpass filter without any downconversion to IF. The second architecture, the indirect (w/ D.C.) MWC, which is also called as QAIC and TS-QAIC [24–26], includes prior downconversion step that shifts down the center frequency of passband sparse signal into IF band. Figs. 4.2 and 4.3 show the examples of the spectra

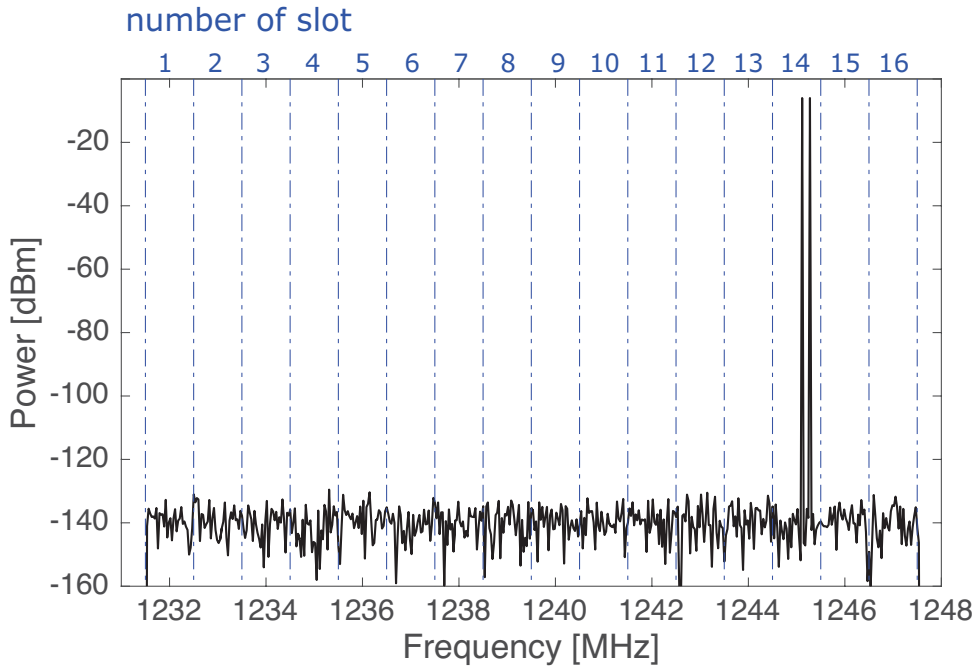

Figure 4.2: Spectrum of sparse wideband signal for direct (w/o D.C.) MWC ($L = 32,\ N = 2$).

of wideband sparse signals with only one active band out of 16 slots within the band of interest ($L = 32$ including the negative frequencies). Each active band includes a multi-tone signal that randomly lies within $B = 1\,\text{MHz}$. One of the reason to use the multi-tone signal in the simulation is that its sparsity in the frequency domain. In other words, it has no spectrum leakage to adjacent bands. In Figs. 4.2 and 4.3 there are two tones in the active band. To overcome peak to average power ratio (PAPR) related issues, phases of multi-tone are set optimally based on low-crest factor algorithm [32]. The input SNR is defined by the ratio of input signal power that is assumed to be 0 dBm and thermal noise power which is determined by $-174 + 10\log_{10}NB$ dBm in the experiment just for convenience. These numbers actually do not affect the NF analysis and the simulation results, because the sensing matrix $\mathbf{A}$ is not determined by input signal but by PSF only.

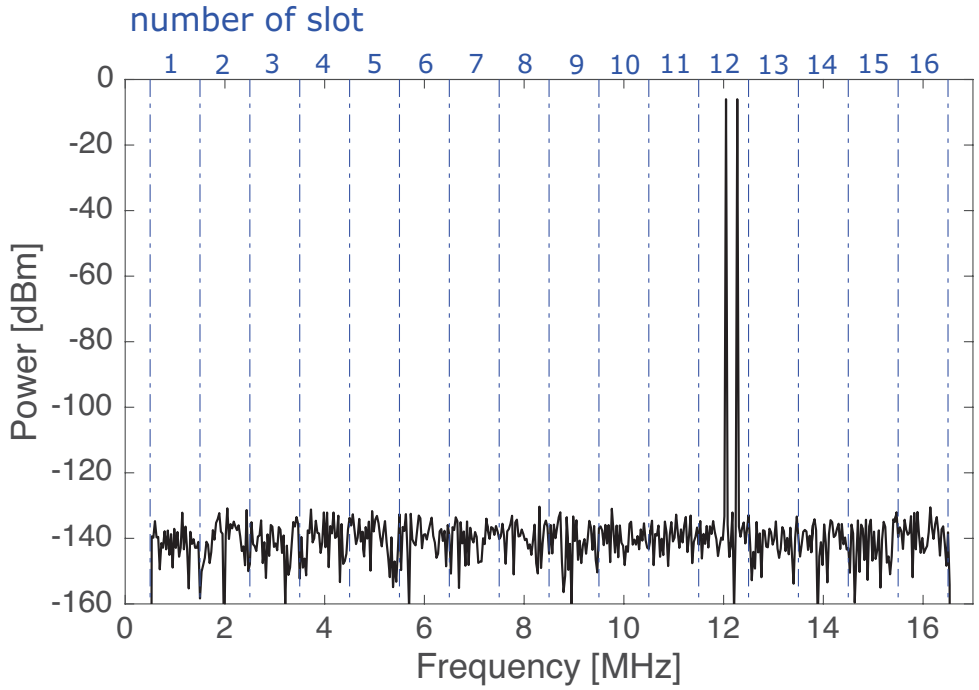

Figure 4.3: Spectrum of sparse wideband signal for indirect (w/ D.C.) MWC ($L = 32,\ N = 2$).

4.2.2 Reconstruction of Sparse Signal in MWC and NF Calculation

Figs. 4.4 and 4.5 present the spectra of the input original and reconstructed signals. Here, the noise floor is gained by some amount due to aliased noise while the signal power retains at the same level on the reconstructed signal. Then SNR_{IN} and SNR_{OUT} will be obtained within $NB = 2\,\text{MHz}$ bands including conjugate band. Figs. 4.6 and 4.7 show time-domain waveforms of the original and the reconstructed signals. Since the input signal contains two tones, the time-domain signal is a sinewave with changing envelope in a narrow time span. Even though the noise floor is gained, it is still imperceptible in the time-domain. Thus the reconstructed signal perfectly matches with the original signal in Figs. 4.6 and 4.7. The NF is obtained from the difference between $SNR_{\text{IN,dB}}$ and $SNR_{\text{OUT,dB}}$ which are taken from the simulation. Then the simulation result of the NF will be compared with our analysis result that is calculated from (4.23). The calculation process based on (4.23) is as follows: First, we derive matrix $\mathbf{A}$ based on the Fourier series coefficients of

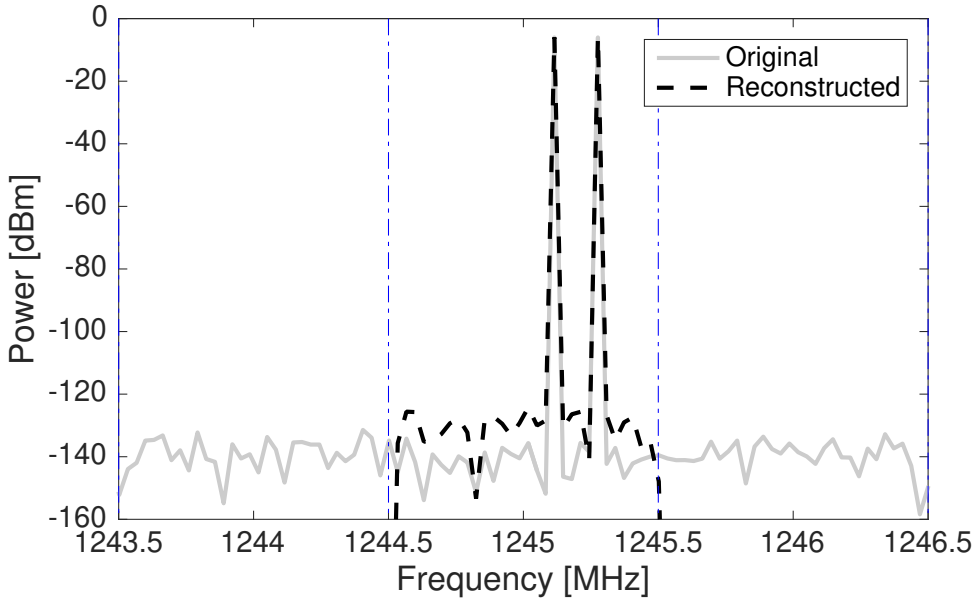

Figure 4.4: Spectrum of sparse wideband signal for direct (w/o D.C.) MWC and reconstructed signal ($L = 32,\ N = 2$).

the used PSFs. Next, we extract the matrix $\mathbf{A}_\mathbf{S}^\dagger$ through the pseudo-inverse operation of the reduced matrix $\mathbf{A}_\mathbf{S}$. Consequently, the matrix multiplication is performed between $\mathbf{A}_\mathbf{S}^\dagger$ and $\mathbf{A}$ matrices as given by (4.23), then the matrix norm (4.9) of the product gives noise factor of the MWC system. When the design parameters for MWC and input signal parameters are respectively set with $m = 2,\ M = 161,\ f_p = 1$ MHz, $f_c = 161$ MHz and $L = 32,\ N = 2$, Fourier series coefficients of the PSF for direct (w/o D.C.) and indirect (w/ D.C. by 2410 MHz local oscillator) MWC can be found in Figs. 4.8 and 4.9, respectively. As illustrated in Fig. 4.8, PSF coefficients at high-frequencies within the band of interest $2411 - 2426$ MHz carry out the downconversion of the incoming signal by the mixer for the direct MWC. On the other hand, the indirect MWC downconverts the incoming signal prior to the MWC, and thus PSF coefficients at low-frequencies in the range of $1 - 16$ MHz are exploited as shown in Fig. 4.9. So even with the same PSF sequences the set of coefficients are different. The total NF from the simulation are plotted in Figs. 4.10 and 4.11. Here we find that the $\mathrm{NF}_{\mathrm{TOTAL}}$ is extremely high when a frequency index $j = 2415$ for w/o D.C. case as illustrated in Fig. 4.10. The reason is clearly seen in the zoom-in view of Fig. 4.8, which has nearly zero amplitude for the

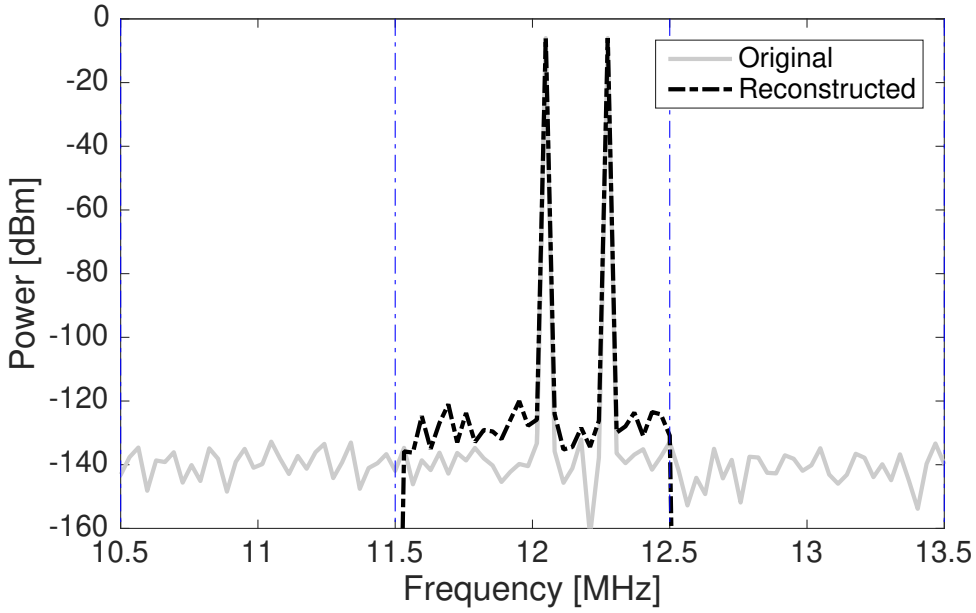

Figure 4.5: Spectrum of sparse wideband signal for indirect (w/ D.C.) MWC and reconstructed signal ($L = 32,\ N = 2$).

downconversion of the corresponding signal. That zero-crossing of PSF spectrum occurs at every integer multiple of $M/T_P = f_c$. Hence, the number of symbols M of PSF must be carefully chosen such that these zero-crossings is not located within the band of interest, while it preserves necessary condition $M \geq L$ [7]. In order to have the zero-crossing out of the band of interest, M can be increased to make the distance between two zero-crossings far-off. However, M can not be exceedingly large as it may increase the hardware complexity for the PSF generation. In the case of indirect (w/ D.C.) MWC or MWC with prior downconversion, the above condition is automatically satisfied through $M \geq L$, the necessary condition from [7]. Therefore there is no such an issue in Fig. 4.11. To avoid the zero-crossing points in Fig. 4.8, M is changed into 159 so that the PSF spectrum does not have a zero amplitude within the band of interest ($2410 - 2426$ MHz) as shown in Fig. 4.12. Then NF on all frequencies become applicable as shown in Fig. 4.13. But still, these noise figures can be high when the number of channels m is just met on necessary condition. One of the straightforward ways to reduce the NF is to increase the number of channels m by using more hardware. In other words, the increment of m expands the matrix sizes of (4.23) to increase the number of measurements so that the noise is more

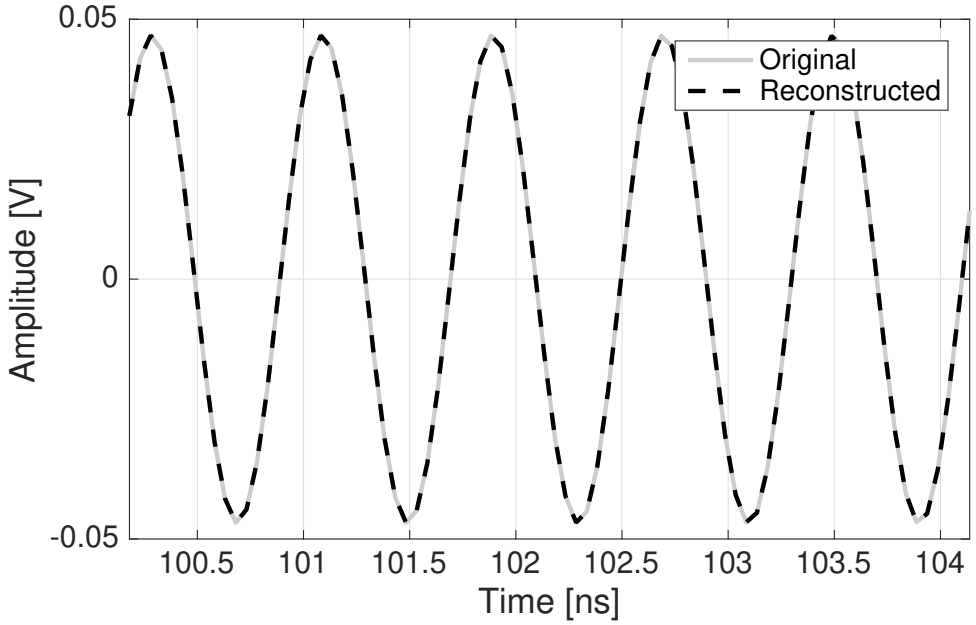

Figure 4.6: Time-domain waveform of sparse wideband signal for direct (w/o D.C.) MWC and reconstructed signal ($L = 32,\ N = 2$).

averaged then the NF is decreased.

4.2.3 Average Noise Figure (ANF) of MWC

In order to compare different settings and cases, average noise figure notation is used in the following simulations that averages the F over every frequency within the band of interest. Also the more feasible ANF can be achieved with Monte Carlo simulations with different PSF for each simulation.

Fig. 4.14 illustrates ANF of direct (w/o D.C.) and indirect (w/ D.C.) MWC with one active band in the input sparse signal. We swept both m and L parameters in several combinations to plot the graph by sweeping m/L in this experiment. As we can see on the graph, the ANF is a function of the ratio m/L. This is explained in the following way: As L is the number of slots within the band of interest, increasing L simply increases the total bandwidth that leads to a linear increase in thermal noise power accumulated at the baseband. Increasing the number of channels m, on the other hand, is effectively the same as increasing the number of measurements. Thus after the matrix operation in the digital domain, the signal power, which is correlated among all the channels, increases with m^2

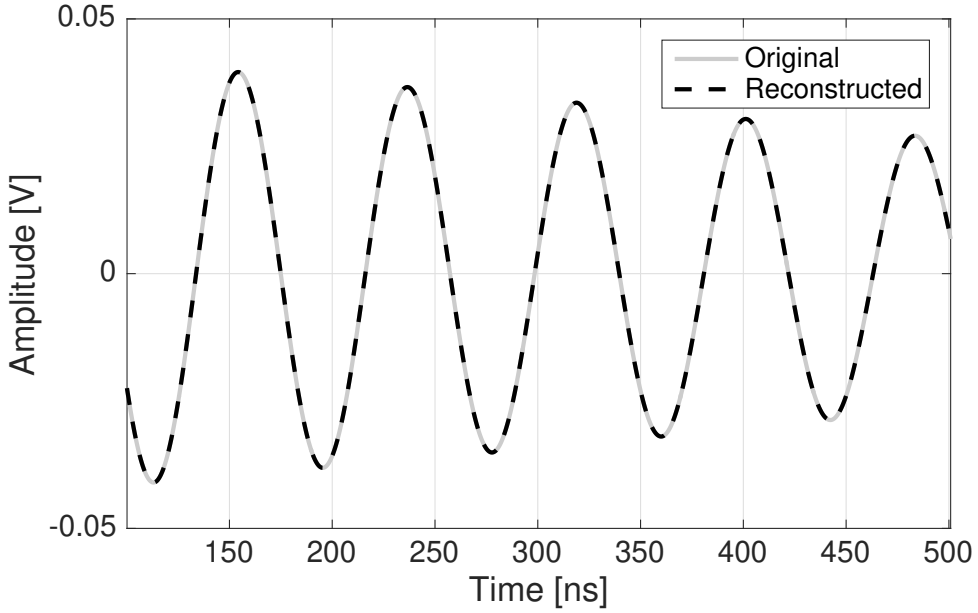

Figure 4.7: Time-domain waveform of sparse wideband signal for indirect (w/ D.C.) MWC and reconstructed signal ($L = 32,\ N = 2$).

while the noise power, which is uncorrelated, increases linearly with m. This results in a linear improvement in NF along with m. Therefore, as demonstrated in Fig. 4.14, the ANF of the MWC depends on m/L. There is actually no difference between the ANF results in two cases of MWC systems shown in Fig. 4.1 as expected by (4.23). In all cases, our analysis well predicts the simulated ANF of the MWC. The green dotted line shows the theoretical limitation, which has a $-3\,\mathrm{dB/octave}$ slope [35] in $m \leq L$ region while constant $0\,\mathrm{dB}$ in $m \geq L$ region. In the example of $L = 1$, $m = 1$, the input signal that has only one active band including noise is located at baseband below $B/2$ bandwidth and only one ADC samples the input signal. In this case, if there is no quantization error on ADC, NF will be 0 dB. In general, a multi-band signal ($N > 2$) is more realistic sparse signal for the MWC system. Fig. 4.15 summarizes the comparison in the cases with $N = 4$ and $N = 6$. It demonstrates that the ANF stays the same as long as MWC has necessary number of channels $m \geq 2N$ even for a multi-band signal.

Fig. 4.16 shows the ANF of the overall systems including practical analog front-end components. Supposing the architectures shown in Fig. 4.1, we assumed to use a BPF with $-0.9\,\mathrm{dB}$ gain and $0.9\,\mathrm{dB}$ NF, a downconverter with $-7.2\,\mathrm{dB}$ conversion gain and $7.3\,\mathrm{dB}$

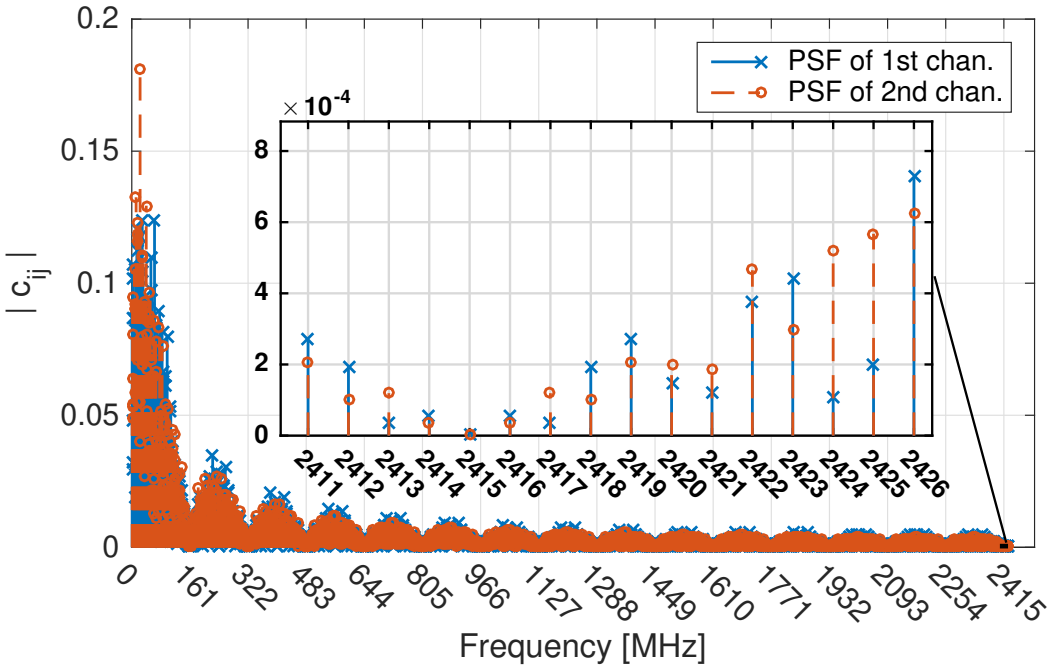

Figure 4.8: Fourier series coefficients of PSF for direct (w/o D.C.) MWC ($L = 32,\ m = 2,\ N = 2,\ M = 161,\ f_c = 161$ MHz).

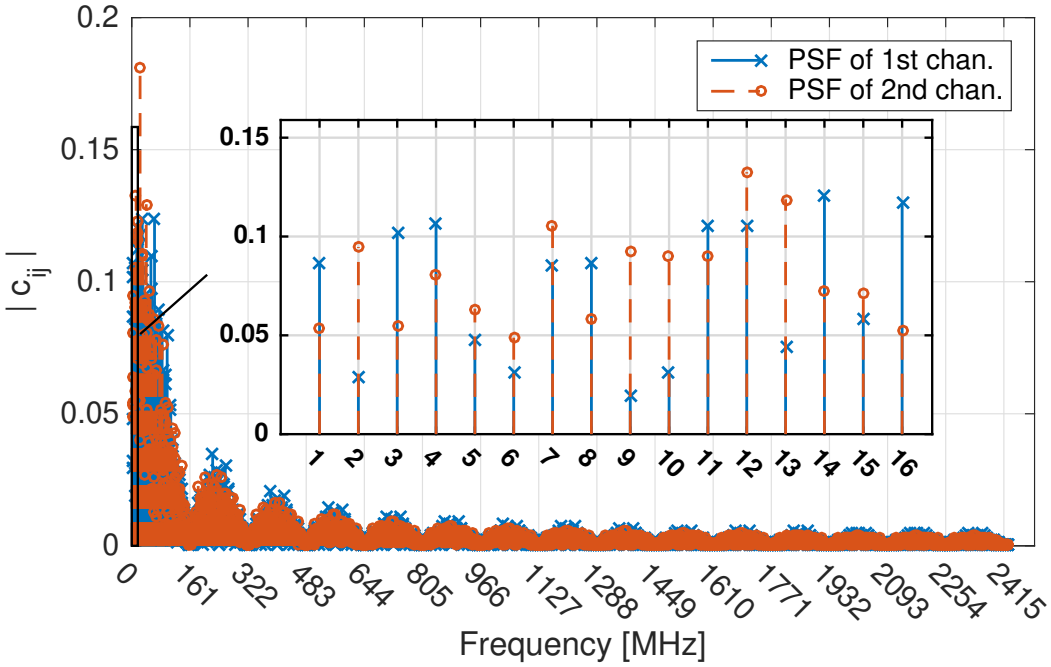

Figure 4.9: Fourier series coefficients of PSF for indirect (w/ D.C.) MWC ($L = 32,\ m = 2,\ N = 2,\ M = 161,\ f_c = 161$ MHz).

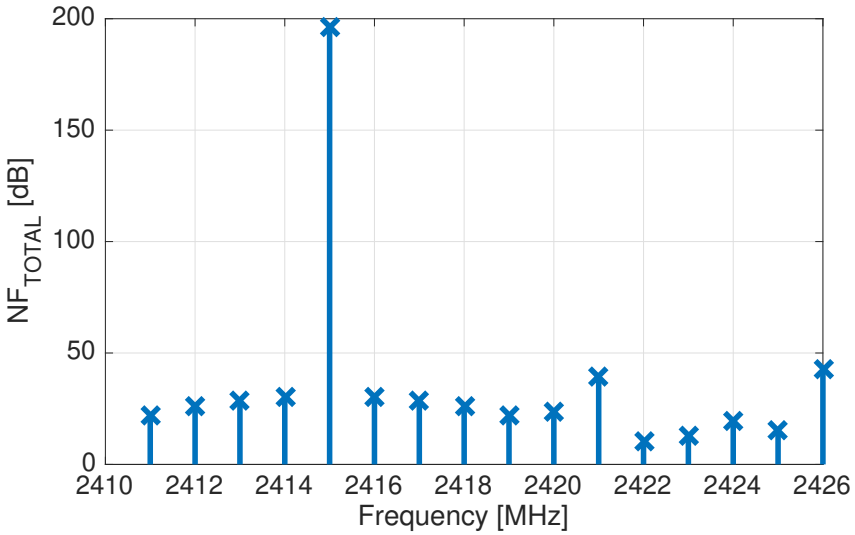

Figure 4.10: Noise figure of direct (w/o D.C.) MWC ($L = 32$, $m = 2$, $N = 2$, $M = 161$, $f_c = 161$ MHz).

NF and an LPF with 7 dB gain and 7.5 dB NF. As for the LNA, we assumed two different performance for comparison: LNA_1 with 31 dB gain and 0.8 dB NF and LNA_2 with 16 dB gain and 1.5 dB NF. The ANF of the overall system is calculated by Friis formula [33]. As in the case with LNA_1, when the front-end LNA has sufficiently high gain and low NF, the ANF of overall system is almost dominated by the LNA performance only. However, with a moderate performance LNA, i.e. LNA_2, depending on the design parameters of the MWC, the noise contribution of the MWC may come into the picture. We can also see the difference in the minimum achievable ANFs between the cases of w/ and w/o D.C. due to the contribution of the downconversion mixer. These results demonstrate that the proposed analysis on the NF of the MWC systems is useful to facilitate the system-level optimization of the MWC-based receiver architectures including the analog front-ends.

4.3 Design Guideline for MWC

According to the analysis and the simulation results that are demonstrated in the previous sections, this section discusses the way to optimize the MWC system in terms of NF. The dominant part of NF is presented in the mixer stage of the MWC that introduces *noise-*

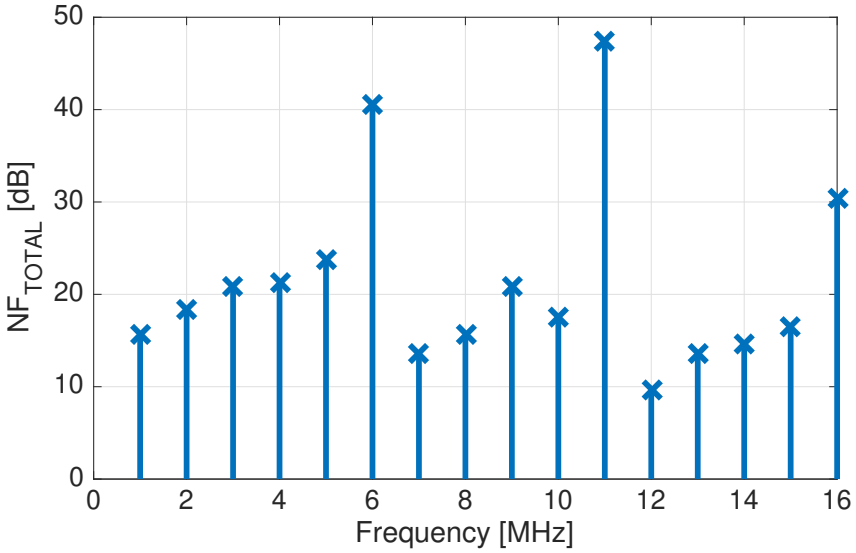

Figure 4.11: Noise figure of indirect (w/ D.C.) MWC ($L = 32,\ m = 2,\ N = 2,\ M = 161,\ f_c = 161$ MHz).

folding effect based on a compressed sensing ratio m/L [35]. In general, the ratio must be defined by

$$\frac{mq}{L} = \frac{mf_s}{Lf_p} \tag{4.25}$$

based on the design parameters in Table 2.1. Thus the number of equivalent analog channels would be mq. Consenquently, we can obtain similar ANF trends of the MWC system as in Figs. 4.14 and 4.15 using mq/L. From the result, it is easily seen that if the number of channels is increased $2\times$, the noise figure of the MWC is improved by 3 dB in the region $m/L < 10^0$. In addition, we can further decrease NF by utilizing parameter q by increasing the sampling rate f_s of the ADCs. Similarly, for the 3 dB improvement in the NF, q also needs to be increased $2\times$. The region $10^0 - 10^2$ in Figs. 4.14 and 4.15 refers that the number of the total channel mq is larger than the number of slots within the band of interest L, which is an inefficient design parameters for MWC even though the ANF of the MWC itself is close to 0 dB. On the other hand, the region $10^{-2} - 10^0$ is realistic choice for practical purpose in terms of hardware efficiency as the NF of the whole system would be improved with appropriate front-end circuits as shown in Fig. 4.16. By using the proposed analysis, we can optimize the noise performance of the entire system with

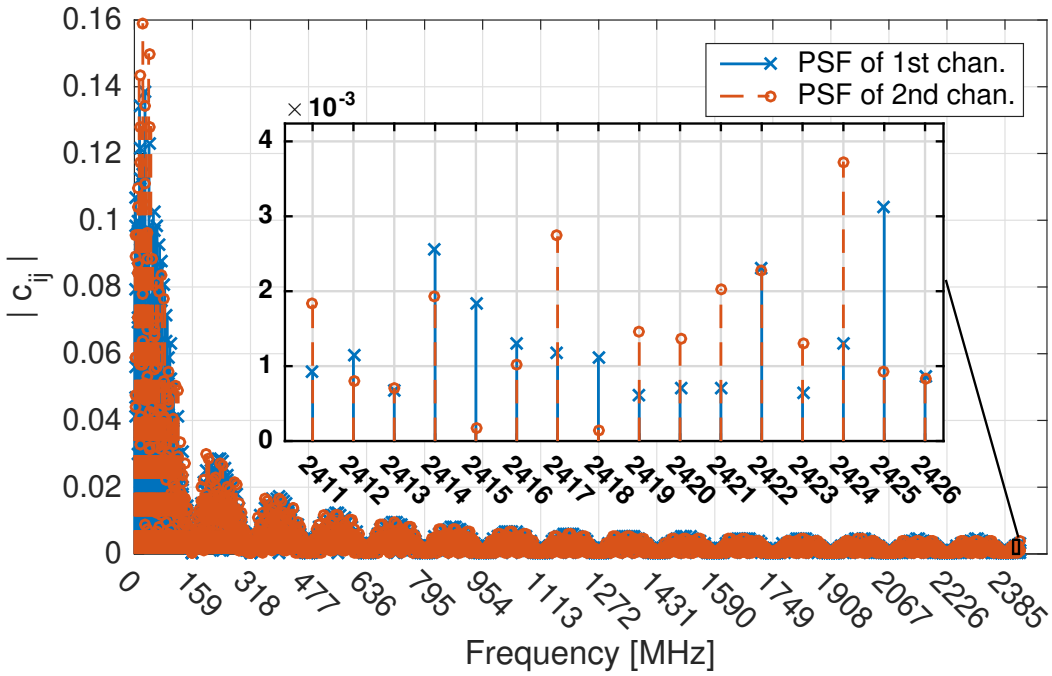

Figure 4.12: Fourier series coefficients of PSF for direct (w/o D.C.) MWC ($L = 32,\ m = 2,\ N = 2,\ M = 159,\ f_c = 159$ MHz).

MWC considering the performance trade-offs such as power consumption and hardware cost. The proposed analysis is also useful to guide the appropriate choice for the building blocks of the MWC systems including analog front ends.

The choice of PSF also affects the ANF of the system. For the case of the MWC w/ D.C., all downconverted signals lie within M/T_p as long as PSF have sufficient $M > L$ symbols in T_p period so that the amplitudes of Fourier series coefficients of the PSF are guaranteed to be nonzeros. However, for the case of the MWC w/o D.C. M must be chosen carefully because Fourier series coefficients of PSF have zero values on kM/T_p for any integer k, as explained in Sect. 4.2.2. The band of interest should not include the zero values otherwise a signal that corresponds to this zero cannot be reconstructed. In the practical implementation of the MWC, the actual NF tends to be degraded from the theoretically estimated NF due to the non-ideality of the hardware components, which affects the actual PSF and whole system's transfer function and leads to deviation on the sensing matrix $\mathbf{A}$ compared to the theoretical definition. As we have demonstrated in the

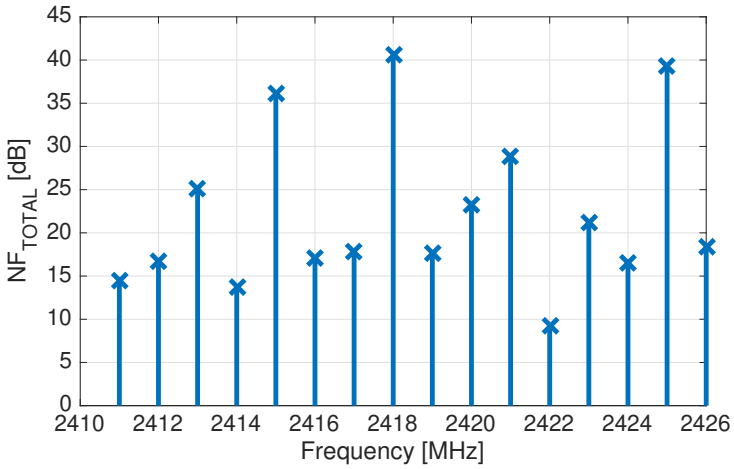

Figure 4.13: Noise figure of direct (w/o D.C.) MWC ($L = 32, m = 2, N = 2, M = 159,\ f_c = 159$ MHz).

previous section, however, the analytical ways to predict the performance that guide the design choice are essential to achieve system-level optimization especially at the initial design stage.

4.4 Summary

The NF of an MWC is analytically investigated in this thesis. The simulation result shows that the analytic noise figure successfully estimates the simulated NF of MWC, which is created with different design parameters. The analysis and the simulation results show that MWC-based architectures in Fig. 4.1 have similar noise figures when all ADCs are assumed to be ideal. In the practical case, as the sampling rate and the number of channels are limited, most MWC-based applications such as spectrum analyzer and cognitive radio have great interest on the region $m \ll L$. Even though the noise figure of the MWC becomes considerably high when $m \ll L$, with an appropriate choice of low-NF, high-gain RF front-end circuits the overall noise figure can be reduced to target specification. The proposed theoretical analysis on NF of the MWC systems will facilitate the system-level optimization of the MWC-based receiver architectures in terms of noise performance.

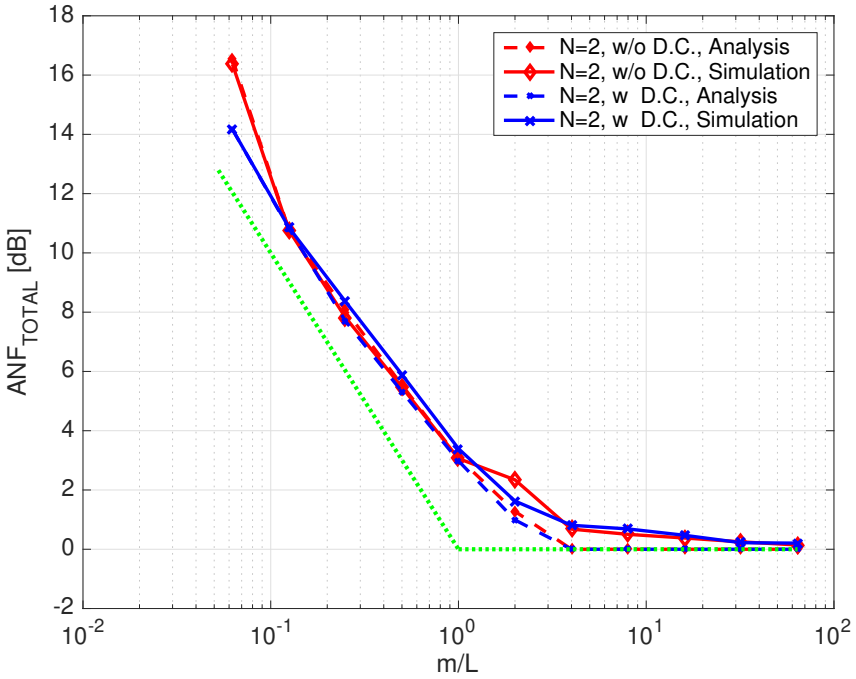

Figure 4.14: Comparison of MWC ANF between analysis and simulation results depending on m/L that indicates compressed sensing ratio ($N = 2$).

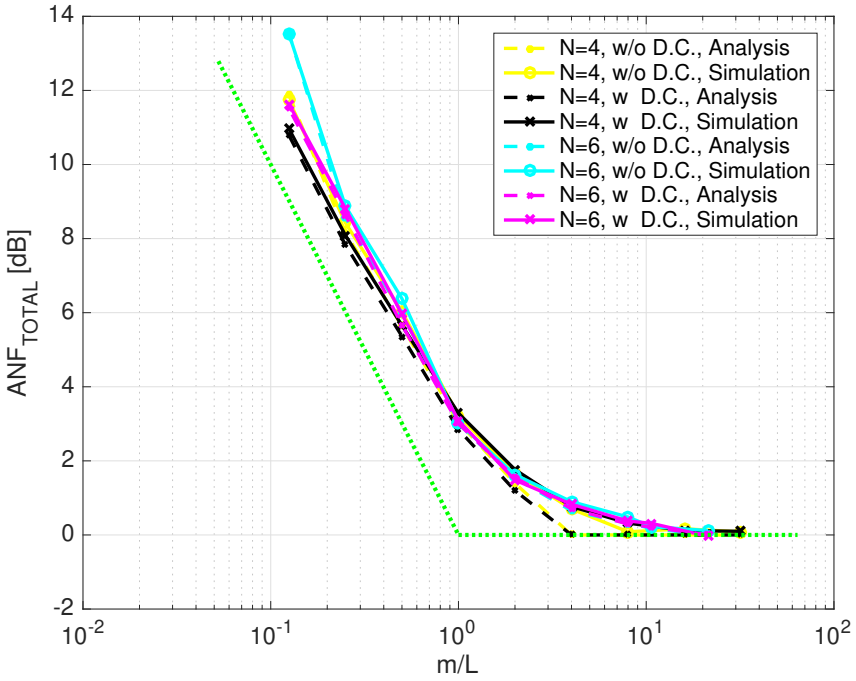

Figure 4.15: Comparison of MWC ANF between analysis and simulation results depending on m/L that indicates compressed sensing ratio ($N = 4, 6$).

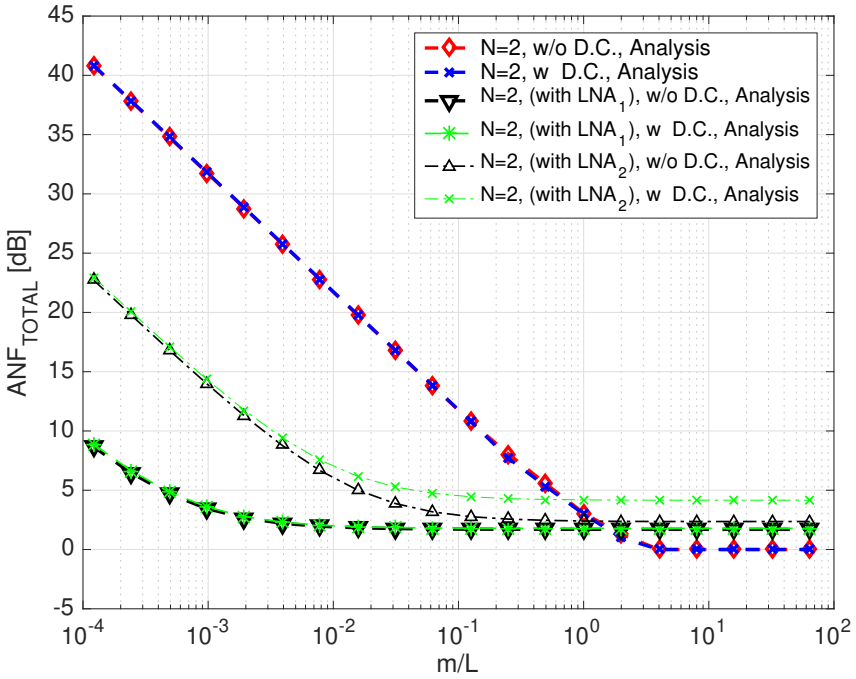

Figure 4.16: ANF of overall system with hypothetical analog front-ends used in front of MWC ($N = 2$).

Chapter 5

Advanced Digital Compensation Filter Design for Digital Pre-Processing of MWC

This chapter is removed in this abridged version.

5.1 Prior Related Works

This section is removed in this abridged version.

5.2 Non-ideal Frequency Characteristic Model of the MWC

This section is removed in this abridged version.

5.3 Proposed Digital Compensation Filter

This section is removed in this abridged version.

5.4 Compensation Performance

This section is removed in this abridged version.

5.5 Summary

This section is removed in this abridged version.

Chapter 6

Calibration Techniques of Sensing Matrix in MWC

The recovery process and the reconstruction procedure for the sensed multiband sparse signal is ideally well-defined by sensing matrix of the compressed sensing in mathematical frameworks, the existing implementations including quadrature analog-to-information converter (QAIC), time-segmented QAIC (TS-QAIC) and random triggering based modulated wideband compressive sampling (RT-MWCS) in [36] , [10, 11, 14, 15, 36–45] face several practical issues related to the non-ideality of the analog components including mixer, low-pass filter (LPF) and analog-to-digital converter (ADC) that cause uncertain deviation on the sensing matrix from its ideal value. Without calibrating the sensing matrix, realization of the reconstruction and the recovery of support becomes infeasible. The previous works [13–15, 36, 37, 46, 47] exploit the estimation method for actual sensing matrix based on a set of sequential measurements of single-tones with known frequencies. This iterative method is extremely time-consuming and the digital processing of the calibration turns into computationally complex due to the large number of calibration signals for real-time applications. In addition, the accuracy of the calibration may be deteriorated by the measurement-to-measurement timing mismatch.

6.1 Conventional Calibration Method for the MWC

In this section, two different conventional calibration methods based on the single-tone training signal are introduced. The single-tone training signal can be written as

$$\tilde{x} = \cos(2\pi f_t t), \tag{6.1}$$

where f_t is the frequency of the training signal. Depending on the choice of the f_t, two different calibration methods are introduced by the literatures [15, 46].

6.1.1 Case $f_t = kf_p,\ k \in \mathbb{Z}$

The literature [46] proposed the calibration method based on the single-tone training signal. The frequency of the training signal is iteratively adjusted with $f = 2\pi k f_p$ where $1 \leq k \leq L_0$. The training signal is defined by

$$\tilde{x}(t) = \cos(2\pi(kf_p)t). \tag{6.2}$$

After the MWC processes, the sampled signal in the i-th channel is written as

$$\tilde{y}_i[n] = \frac{1}{2}(c_{i,k} + c_{i,-k}). \tag{6.3}$$

Considering the property $c_{i,k} = c^*_{i,-k}$, the following equation is obtained

$$\mathrm{Re}\{c_{i,-k}\} = \tilde{y}_i[n]. \tag{6.4}$$

Applying similar discussion to $\sin(2\pi(kf_p)t)$ where $1 \leq k \leq L_0$ then the sampled signal in the i-th channel is

$$\tilde{y}_i[n] = \frac{j}{2}(c_{i,k} - c_{i,-k}), \tag{6.5}$$

which leads to

$$\mathrm{Im}\{c_{i,-k}\} = \tilde{y}_i[n]. \tag{6.6}$$

This calibration procedure starts with cosine wave by setting the input frequency to f_p. Then, the real component of $c_{i,-k}$ is directly obtained from the output of the ADC as in (6.4). After that, the input signal is changed into sine wave with the same frequency. In the same manner, the imaginary component of $c_{i,-k}$ is directly obtained from the output of the ADC as in (6.6). From these two measurements, $c_{i,-k}$ is obtained. By iteratively changing the frequency and repeating the procedure, the exact elements in the actual matrix $\mathbf{A}$ can be calculated [46].

This approach needs $2L_0$ measurements for the calibration of actual sensing matrix that may includes measurement-to-measurement timing and gain mismatches due to the uncertainty in the ADC sampling timing, channel-to-channel timing skew of the signal source, etc.

6.1.2 Case $f_t \neq kf_p,\ k \in \mathbb{Z}$

The literature [15] proposed a calibration method based on the single-tone signal as given by

$$\tilde{x} = \sin(2\pi(kf_p + f_0)t), k \in [0, 1, ..., L_0]. \tag{6.7}$$

Here, the bias frequency f_0 is set within the range of $0 < f_0 < f_p/2$. After the MWC processes, the sampled signal in the i-th channel is written as

$$\tilde{y}_i[n] = c_{i,k} \sin(2\pi f_0 n T_s). \tag{6.8}$$

Due to the impact of some added noise and nonlinear effects of the mixer, the $\tilde{y}_i[n]$ contains additional harmonics at DC, bf_p and bf_0 for $b \in \mathbb{N}$. To extract the $c_{i,k}$ term, first they removed DC component by subtracting the mean value of the signal. Then they estimated the actual frequency $\tilde{f}_0$ based on Welch's spectrum estimation [48]. Finally,

they applied a least square method to estimate the $c_{i,k}$ based on

$$\underset{c_{i,k}}{\operatorname{argmin}} \|\tilde{y}_i[n] - c_{i,k} \sin(2\pi \tilde{f}_0 n T_s)\|^2. \tag{6.9}$$

After performing $L_0 + 1$ iterations of the above calibration procedure, the sensing matrix is obtained [15]. Using $f_t \neq k f_p, k \in \mathbb{Z}$, the complex number $c_{i,k}$ is obtained from one measurement in this method while the previous method in Sect. 6.1.1 requires two. Thus this approach reduces the total number of measurement to L_0.

6.2 Proposed Calibration Technique

In this section, the proposed calibration technique is explained in comparison to the conventional calibration method as discussed in Sect. 6.1. First, we define a pilot signal that is necessary for the proposed calibration technique. Afterwards, the estimation method of the actual sensing matrix based on the pilot signal is proposed.

6.2.1 Pilot Signal Generation

Although the MWC is designed for wideband sparse signal, we exploit dedicated non-sparse signal for this calibration technique as shown in Fig. 6.1(a). The pilot signal for the calibration is a multi-tones as follows:

$$\tilde{x}(t) = \sum_{l=1}^{L_0} \cos(2\pi(l f_p + f_l)t + \phi_l), \tag{6.10}$$

where ϕ_l is an initial phase and f_l is a pilot single-tone frequency that lies within $f_p/2$. The set of the phases is important to limit the crest factor in order to maximize the dynamic range within a limited full-scale range of the ADC. For this purpose, the Newman phases are used in this thesis to present low crest factor. According to [49], the Newman phases can be given by

$$\phi_l = \frac{\pi(l-1)^2}{L_0}. \tag{6.11}$$

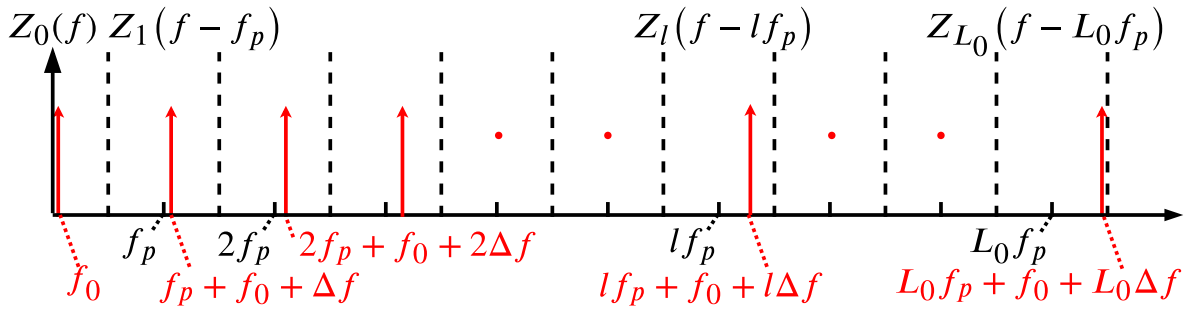

(a)

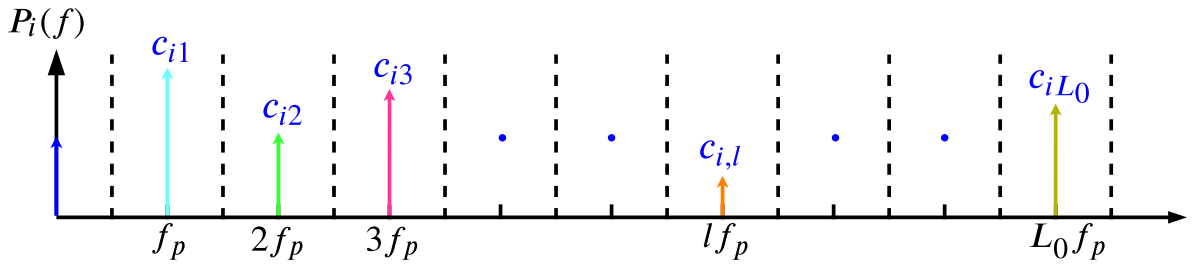

(b)

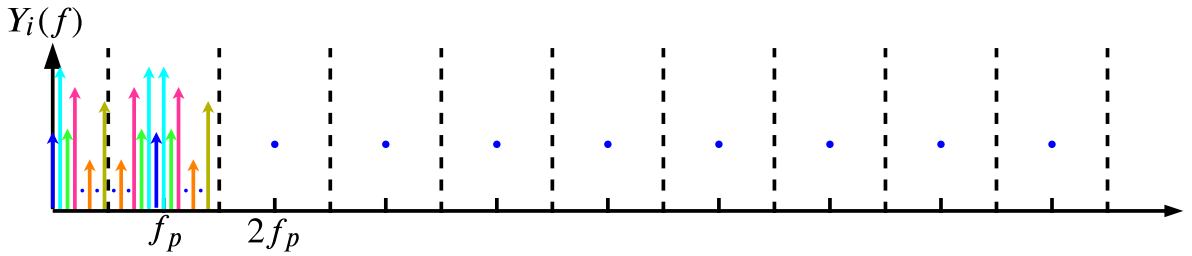

(c)

Figure 6.1: (a) Spectrum of the pilot signal, (b) Fourier series of the i-th PSF, (c) Spectrum of the mixer output.

In more detail on the frequency set, f_l can be linearly spaced for straightforward understanding as

$$f_l = f_0 + l\Delta f. \tag{6.12}$$

Here, f_0 is a offset frequency for all tones, Δf is a constant distance between tones. In the frequency-domain, (6.10) is rewritten as

$$\tilde{X}(f) = \sum_{l=-L_0}^{L_0} \tilde{Z}_l(f - lf_p) = \sum_{l=-L_0}^{L_0} e^{j\phi_l}\delta(f - lf_p - f_l), \tag{6.13}$$

where each $\tilde{Z}_l(f)$ spectrum slice of the input signal contains single-tone at $lf_p + f_l$ as illustrated in Fig. 6.1(a).

6.2.2 MWC with Pilot Signal

In order to identify the actual transfer function deviated due to hardware-related non-idealities, the pilot signal explained above is used as the input to the MWC. The discrete-time Fourier transform of the i-th output (2.4) of the ADC is given by

$$\tilde{Y}_i(e^{jwT_s}) = \sum_{l=-L_0}^{L_0} \tilde{c}_{i,-l}\delta(f - f_l). \tag{6.14}$$

Here, $\tilde{c}_{i,-l}$ is a Fourier series coefficients of the *actual* PSF, which is not equal to the *ideal* $c_{i,-l}$. Each single tone at f_l from each spectrum slice $\tilde{Z}_l(f)$ of the pilot signal in Fig. 6.1(a) is mixed with the corresponding *actual* coefficient $\tilde{c}_{i,-l}$ of the PSF in Fig. 6.1(b) and the downconverted part of the mixer output is illustrated in Fig. 6.1(c). The main advantage of the pilot signal can be seen in (6.14); the downconverted components are disjoint in the frequency-domain. Then (2.6) is rewritten as

$$\tilde{\mathbf{Y}} = \tilde{\mathbf{A}}\tilde{\mathbf{Z}}, \tag{6.15}$$

where $\tilde{\mathbf{Y}} = [\tilde{Y}_1(e^{jwT_s}), \tilde{Y}_2(e^{jwT_s}), ...\tilde{Y}_m(e^{jwT_s})]^T$, $\tilde{\mathbf{Z}} = [\tilde{Z}_{-L_0}(f), ..., \tilde{Z}_{-1}(f), \tilde{Z}_0(f), \tilde{Z}_1(f), ...\tilde{Z}_{L_0}(f)]^T$ and $\tilde{\mathbf{A}}_{i,j} = \tilde{c}_{i,j}$. In other words, $\tilde{Z}_l(f)$ contains only one nonzero component in the frequency domain. Based on this advantage, (6.15) can be rewritten as

$$\tilde{Y}_i(e^{j2\pi f_l T_s}) = [\tilde{\mathbf{A}}]_{i,l}\tilde{Z}_l(f_l), \tag{6.16}$$

so that each component $\tilde{Y}_i$ of $\tilde{\mathbf{Y}}$ is independent of other components of $\tilde{\mathbf{Z}}$ in (6.15).

6.2.3 Calibration of the Actual Sensing Matrix

According to (6.16) and its disjoint feature of the mixer output signal in the frequency-domain, the actual coefficients of the sensing matrix can be independently calculated as

$$\tilde{c}_{i,l} = \frac{\tilde{Y}_i(e^{j2\pi(f_l)T_s})}{\tilde{Z}_l(f_l)} \quad \text{for all} \quad l \in [-L_0, L_0],\ i \in [1, m]. \tag{6.17}$$

The pilot signal is non-sparse as it covers many bands within the frequency of interest, thus the MWC does not have a capability to reconstruct it. However, based on (6.17) the coefficients of the sensing matrix are extracted without reconstructing the original pilot signal. The calculation of the whole sensing matrix coefficients needs only a single measurement with the pilot signal in the proposed calibration method.

The advantages of the proposed calibration technique are summarized as follows:

- The ideal reconstruction of the MWC in [7] assumes that there is no time difference between the PSF and the ADC clock. However, the time difference is introduced by a non-zero wiring delay in the practical implementation. This time difference can be taken into account as a linear phase shift in the sensing matrix as pointed out by [13, 36, 50]. In the proposed technique, the time difference between PSF and ADC clock is automatically included in the *actual* $\tilde{c}_{i,l}$ in (6.17). For example, if a time delay t_i exists between i-th PSF and the ADC clock (explained later in Fig. 7.2(b)), then it introduces additional $e^{j2\pi l f_p t_i}$ phase shift on l-th component $c_{i,l}$ of the PSF. That phase shift will be directly measured by l-th tone of the pilot signal at $lf_p + f_l$ frequency then the mixer downconverts the phase-shifted component into f_l frequency. Therefore the phase shift information appears in $\tilde{Y}_i(e^{j2\pi f_l T_s})$ so that $\tilde{c}_{i,l}$ obtains the $e^{j2\pi l f_p t_i}$ phase shift through (6.17).

- The conventional method does not have a capability to estimate the accurate *initial phase* of the single-tone signal. The reason is that the *initial phase* of the single-tone signal is shifted by the phase characteristics of the transfer function as well as by a measurement-to-measurement timing fluctuation. This timing fluctuation in the

single-tone sequential measurement results in unexpected phase rotations on each sensing matrix coefficient, which in consequence leads to a reconstruction failure. However, in the proposed calibration method, all the coefficients in the sensing matrix is obtained from the single measurement so that the phase rotations of all the coefficients are identical. Even if the sampling timing in the actual measurement is shifted from that in the calibration, it just introduces some time shift in the time-domain waveform, which does not distort the waveform shape. The *initial phase* is also necessary to find the starting point of the signal so that the timing mismatch can be compensated in the multi-channel MWC. The relative phases between tones in the pilot signal are defined by the Newman phases as introduced in Sect. 6.2. Using this relation the *initial phase* of the input signal can be calculated precisely.

- Similar to the initial phase estimation, the gain mismatch of the multi-channel is also detectable based on the pilot signal. These gain and timing mismatches are necessary to be compensated in the multi-channel MWC to avoid a reconstruction failure.

6.2.4 The Reconstruction Performance Based on NMSE and IRR

The quantification of the reconstruction performance of the MWC is necessary to demonstrate the effectiveness of the calibration method. For that reason, the normalized mean square error (NMSE) of the time-domain reconstructed signal $\hat{x}(t)$ with respect to the original input signal $x(t)$ is defined as follows:

$$\mathrm{NMSE}_{\mathrm{dB}} = 10\log_{10}\int_{-\infty}^{\infty}\frac{\|x(t)-\hat{x}(t)\|^2}{\|x(t)\|^2}dt. \tag{6.18}$$

Here, the mean square error (MSE) part in the numerator $\frac{1}{T}\int_0^T \|x(t)-\hat{x}(t)\|^2$ is normalized by the average signal power $\frac{1}{T}\int_0^T \|x(t)\|^2$ in the denominator. As the reconstructed time-domain waveform $\hat{x}(t)$ approaches closer to the original input waveform $x(t)$, the

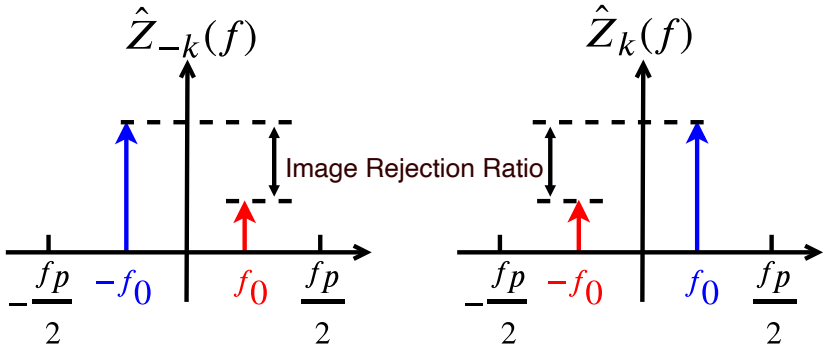

Figure 6.2: The reconstructed original single-tone and its unwanted image are highlighted as blue circles and red triangles in the frequency-domain, respectively.

MSE part reaches to 0 then NMSE in decibel goes to minus direction.

The alternative way to quantify the reconstruction performance is an image rejection ratio (IRR). The actual sensing matrix $\tilde{\mathbf{A}}$ is no longer an inverse of the ideal $\mathbf{A}_\mathbf{S}^\dagger$ that results in $\mathbf{A}_\mathbf{S}^\dagger \tilde{\mathbf{A}} \mathbf{Z} \neq \mathbf{Z}_\mathbf{S}$. In more detail, the image is introduced when the single-tone is injected. Supposing that the input single-tone is given by

$$x(t) = \cos(2\pi(kf_p + f_0)t), \tag{6.19}$$

where $f_0 < f_p/2$, its frequency-domain components are defined as

$$X(f) = \frac{1}{2}(\delta(f - kf_p - f_0) + \delta(f + kf_p + f_0)) \tag{6.20}$$

such that $\mathbf{S} = \{-k, k\}$. Then the nonzero spectrum slices of the input signal as in (2.2) is given by

$$Z_k(f) = \frac{1}{2}\delta(f - f_0) \tag{6.21}$$

$$Z_{-k}(f) = \frac{1}{2}\delta(f + f_0) \tag{6.22}$$

Recalling (2.4), the i-th digital output of the ADC in the MWC is expressed by

$$\begin{aligned} Y_i(e^{jwT_s}) &= \tilde{c}_{i,-k}Z_k(f) + \tilde{c}_{i,k}Z_{-k}(f) && (6.23)\\ &= \frac{1}{2}(\tilde{c}_{i,-k}\delta(f-f_0) + \tilde{c}_{i,k}\delta(f+f_0)). && (6.24)\end{aligned}$$

After the reconstruction as in (2.9) with $m = 2$ case, the reconstructed spectrum slices are given by

$$\begin{aligned} \hat{Z}_k(f) &= \frac{1}{2}[\mathbf{A}_\mathbf{S}^\dagger]_{1,1}(\tilde{c}_{1,-k}\delta(f-f_0) + \tilde{c}_{1,k}\delta(f+f_0))\\ &+ \frac{1}{2}[\mathbf{A}_\mathbf{S}^\dagger]_{1,2}(\tilde{c}_{2,-k}\delta(f-f_0) + \tilde{c}_{2,k}\delta(f+f_0)), && (6.25)\end{aligned}$$

which leads to

$$\begin{aligned} \hat{Z}_k(f) &= \frac{1}{2}([\mathbf{A}_\mathbf{S}^\dagger]_{1,1}\tilde{c}_{1,-k} + [\mathbf{A}_\mathbf{S}^\dagger]_{1,2}\tilde{c}_{2,-k})\delta(f-f_0)\\ &+ \frac{1}{2}([\mathbf{A}_\mathbf{S}^\dagger]_{1,1}\tilde{c}_{1,k} + [\mathbf{A}_\mathbf{S}^\dagger]_{1,2}\tilde{c}_{2,k})\delta(f+f_0). && (6.26)\end{aligned}$$

Assuming the ideal case where

$$\begin{aligned} ([\mathbf{A}_\mathbf{S}^\dagger]_{1,1}c_{1,-k} + [\mathbf{A}_\mathbf{S}^\dagger]_{1,2}c_{2,-k}) &= 1\\ ([\mathbf{A}_\mathbf{S}^\dagger]_{1,1}c_{1,k} + [\mathbf{A}_\mathbf{S}^\dagger]_{1,2}c_{2,k}) &= 0, && (6.27)\end{aligned}$$

the reconstructed spectrum results in

$$\hat{Z}_k(f) = \frac{1}{2}\delta(f-f_0). \quad (6.28)$$

Here the image component $\delta(f+f_0)$ is completely rejected. However, considering $\tilde{c}_{i,l} \neq c_{i,l}$

in the practical case, (6.27) is no longer true where

$$[\mathbf{A}_{\mathbf{S}}^{\dagger}]_{1,1}\tilde{c}_{1,-k} + [\mathbf{A}_{\mathbf{S}}^{\dagger}]_{1,2}\tilde{c}_{2,-k} \neq 1, \tag{6.29}$$

$$[\mathbf{A}_{\mathbf{S}}^{\dagger}]_{1,1}\tilde{c}_{1,k} + [\mathbf{A}_{\mathbf{S}}^{\dagger}]_{1,2}\tilde{c}_{2,k} \neq 0. \tag{6.30}$$

Consequently, $\delta(f + f_0)$ is not completely suppressed and it appears on the reconstructed $\hat{Z}_k(f)$ spectrum slice as an image of the original component $\delta(f - f_0)$ as illustrated in Fig. 6.2. The image rejection ratio (IRR) in Fig. 6.2 is defined by

$$\mathrm{IRR}_{\mathrm{dB}} = 10\log_{10}\frac{\|Z_k(f_0)\|^2}{\|Z_k(-f_0)\|^2}, \tag{6.31}$$

which is a power ratio of the original and the image components. In the case of $m = 2$, the IRR is given by

$$\mathrm{IRR}_{\mathrm{dB}} = 10\log_{10}\frac{\left\|[\mathbf{A}_{\mathbf{S}}^{\dagger}]_{1,1}\tilde{c}_{1,-k} + [\mathbf{A}_{\mathbf{S}}^{\dagger}]_{1,2}\tilde{c}_{2,-k}\right\|^2}{\left\|[\mathbf{A}_{\mathbf{S}}^{\dagger}]_{1,1}\tilde{c}_{1,k} + [\mathbf{A}_{\mathbf{S}}^{\dagger}]_{1,2}\tilde{c}_{2,k}\right\|^2}. \tag{6.32}$$

The deviated sensing matrix deteriorates the reconstruction by introducing images of the original signal. To quantify such distortion, the IRR measures the ratio of the image signal power and original signal power regardless of any other components in the frequency domain. The IRR differs from the NMSE by measuring the reconstruction performance in the frequency domain while the NMSE is calculated in the time domain.

6.3 Proposed Calibration Technique with Non-Uniformly Spaced Frequencies

This section is removed in this abridged version.

6.3.1 Simulation Results

This section is removed in this abridged version.

6.3.2 Reconstruction of the Test Signal

This section is removed in this abridged version.

6.4 Summary

The conventional calibration method repeats many measurements with single-tone signals to estimate the actual sensing matrix. However, our proposed calibration needs only a single measurement to estimate all the sensing matrix coefficients at once. It is worth to point out that the IRR is based only on the amplitude spectrum while the NMSE includes phase differences. The main reason that the average IRR of the proposed calibration with uniform frequencies is lower than the conventional method is that the multi-tone signal does suffer from non-linearity.

Chapter 7

Practical Implementation and Measurement Results of MWC Reconstruction Performance

In this section, the proposed calibration method explained in Sect. 6.2 is deployed to a practical implementation setup of the MWC.

7.1 Implementation Setup and MWC Design Parameters

The MWC implementation setup is depicted in Fig. 7.1 and the measurement setup is shown in Fig. 7.2(a). The timing diagram of the measurement setup is illustrated in Fig. 7.2(b). t_i is a time difference between the PSF and the ADC clock in i-th channel. $t_{d,cal}$ is a time difference between the start of the calibration signal and the PSF and $t_{d,meas}$ is a time difference between the start of the actual input signal and the PSF. These unwanted time differences are unavoidable due to the actual measurement setup such as cable delays and timing skews of the measurement equipments. We are providing a single pulse as the trigger signal that controls the logic analyzer to start the measurement.

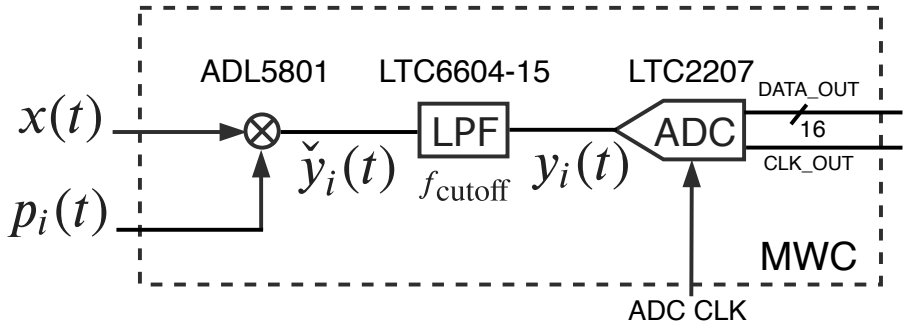

Figure 7.1: The MWC implementation setup

Table 7.1: The design parameters of MWC implementation

Implementation Design Parameters	Notation	Value
Periodic Sign Function (PSF) frequency	f_p	1 MHz
Number of active bands	N	2
Number of slots in band of interest	L	160
Band of interest	W	160 MHz
Bandwidth of active band	B	1 MHz
Number of symbols in PSF	M	500
Number of channels	m	4
Carrier Frequencies	f_i	$(11 - 90)$ MHz
Number of digital channels	q	17
Sampling rate of ADC	f_s	100 MHz
Number of bits on ADC	NOB	16 bits

First of all, t_i is one of the important non-ideal factors that introduces phase deviation on the actual sensing matrix and how it is compensated in the calibration is explained in Sect. 6.2.3. The $t_{d,cal}$ in the proposed calibration introduces just a linear phase shift on the sensing matrix. Even though the $t_{d,cal}$ is not guaranteed to be the same as $t_{d,meas}$ in the actual measurement procedure, such delay has no effect on the sensing matrix but results in a simple time shift in the reconstructed time-domain waveform. On the other hand, the $t_{d,cal}$ in the conventional method throughout all the sequential measurements may be fluctuated. These fluctuations result in different phase shift in each coefficient that introduces distortion on the reconstructed time-domain waveform, not just a simple time shift.

The design parameters of the MWC are summarized in Table 7.1. Note that N, L, M parameters count conjugate frequency components as well.

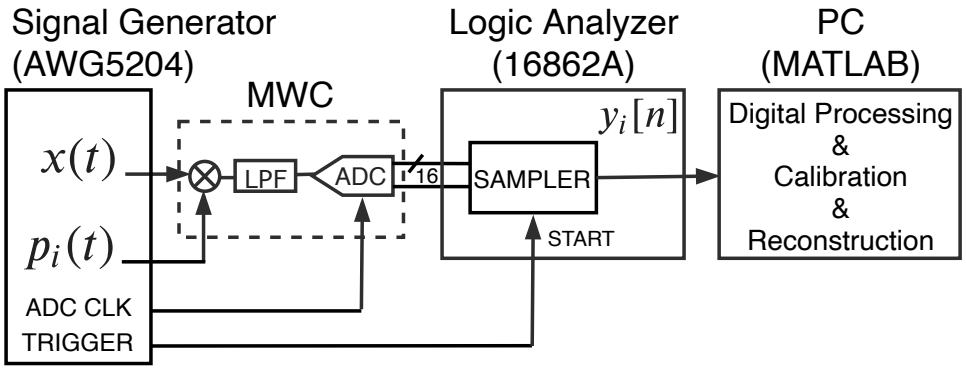

(a)

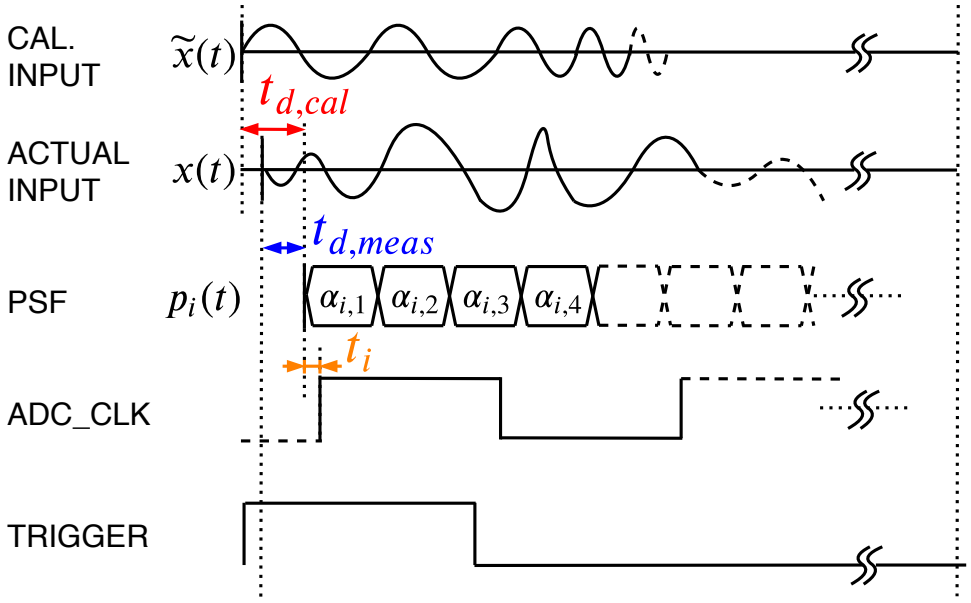

(b)

Figure 7.2: (a) The measurement setup and (b) its timing diagram. t_i is the time difference between the PSF and the ADC clock in i-th channel. $t_{d,cal}$ and $t_{d,meas}$ are the time differences of the calibration input and the actual measurement input relative to the PSF, respectively.

a. Analog mixer

One of the most crucial components in the MWC system is an analog mixer that must have a capability to accept wideband local oscillator (LO) input signal. The reason is that the nature of the MWC system needs to mix the radio frequency (RF) input signal with the PSF that occupies wide bandwidth. However, most of the typical analog mixer is designed to be used with single-tone LO signal. For this realization, the high third-order intercept point (IP3) active mixer ADL5801 [51] is used in this thesis. Its frequency range is sufficiently large from 10 MHz to 6 GHz.

b. Low-pass filter (LPF)

A fully differential 15 MHz 4-th order low-pass filter LTC6604-15 [52] is used as the LPF.

c. ADC

A 16-bits, 105 MS/s ADC, LTC2207 [53] is selected for the high-precision measurement. The sampling speed is set to 100 MHz in this measurement as shown in Table 7.1. The parallel digital output is read by the logic analyzer to export the measured data. Afterward, the digital domain processing and the reconstruction is carried out in MATLAB environment.

d. Emulation of multi-channel MWC

We emulate the multi-channel MWC using a single-channel MWC by taking multiple measurements with different PSFs.

The test signals including the pilot signal, the PSF and the ADC clock were delivered by an arbitrary waveform generator (AWG, Tektronix AWG5204) that supports 4 differential outputs at 5 GHz sampling rate. The waveform files were generated in MATLAB environment in advance. The synchronization signal and 10 MHz clock signal are also distributed by the AWG to the logic analyzer (Keysight 16862A) for synchronization purpose.

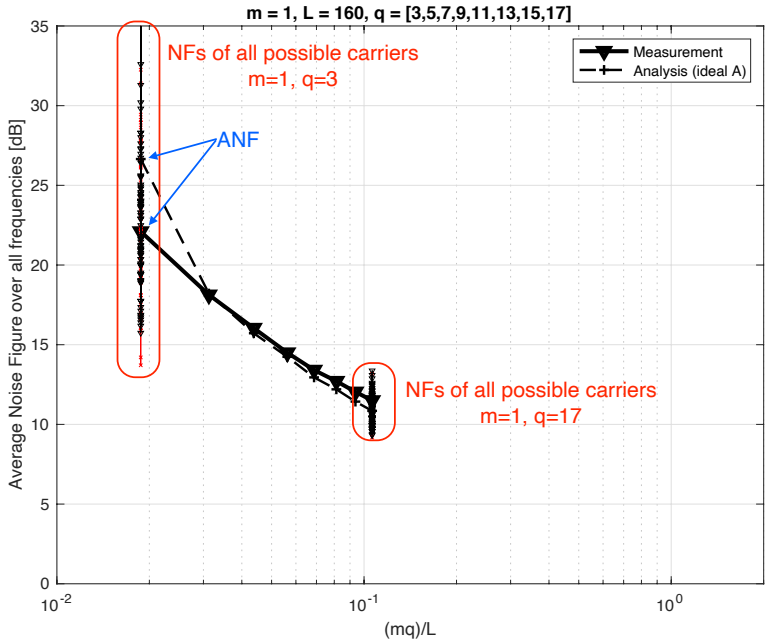

Figure 7.3: Comparison of the single-channel ($m = 1$) MWC ANF between analysis and measurement results depending on mq/L that indicates compressed sensing ratio ($N = 2$).

7.2 Noise Figure Measurement

Figs. 7.3 and 7.4 show the measurement results of the single-channel advanced MWC ($m = 1, q > 1$) and the emulated multi-channel advanced MWC ($m = 4, q > 1$), respectively. We swept both m and q parameters in several combinations to plot the graph by sweeping mq/L in the measurement. In these graphs, we can see that the ANF calculated based on our analysis agrees well with the actual measured value even when the design parameters are changed. It can also be seen that the variation of NF over all carrier frequencies is intensely high when the number of measurements (mq) is insufficiently low relative to L. The reason is that the NF strongly depends on the magnitude of corresponding Fourier series coefficient of the PSF and also the size of sensing matrix is inadequately small, which results in unstable reconstruction. That is why the ANF has some discrepancy when the compressed sensing ratio mq/L is small. On the other hand, as the number of measurements increases relative to L, the variation of NF is reduced.

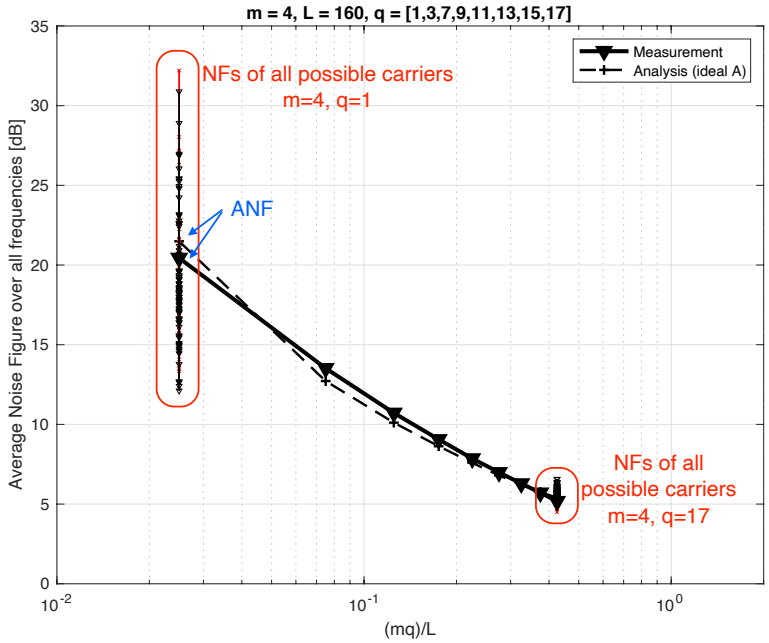

Figure 7.4: Comparison of the multi-channel ($m = 4$) MWC ANF between analysis and measurement results depending on mq/L that indicates compressed sensing ratio ($N = 2$).

7.3 Construction of Compensation Filter

This section is removed in this abridged version.

7.3.1 Calibration Procedure

As previously discussed in Sect. 6.2, the calibration of the actual sensing matrix is carried out using the non-sparse pilot signal. To generate the multi-tones, we may need an AWG equipment rather than a simple sinewave generator. For the experimental comparison, we implemented the conventional calibration method explained in Sect. 6.1.2 as well as the proposed method. The maximum amplitude of the multi-tone pilot signal in the proposed method is set equal to the amplitude of the single-tones in the conventional method in the following experiment.

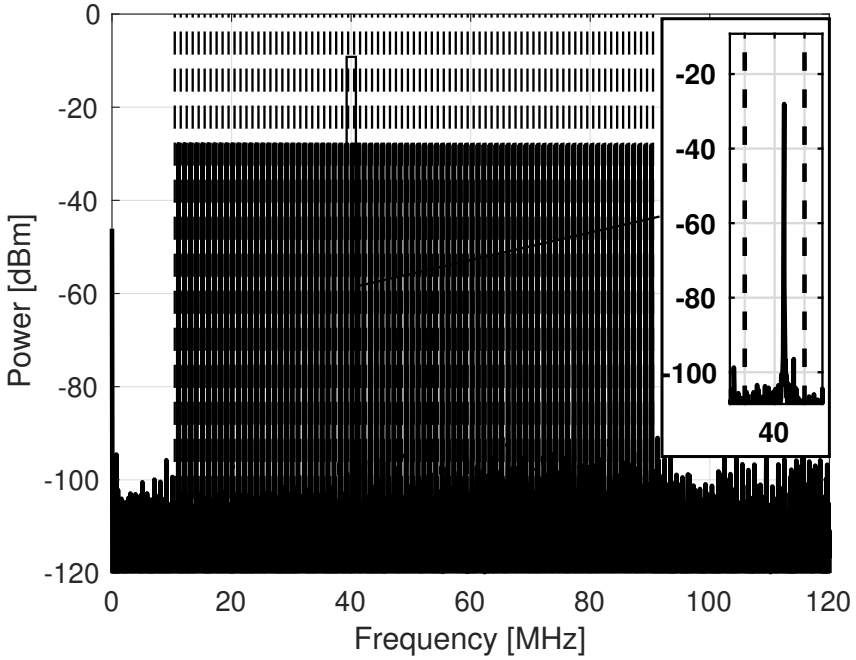

Figure 7.5: Frequency-domain spectrum of the measured pilot signal. In the zoomed-in view, the single-tone resides within the single band as defined in Sect. 6.2.1.

a. Pilot signal generation

The pilot signal is delivered by the AWG. The number of tones 80 excluding conjugate components is set to be the same as the number of the slots within the band of interest as summarized in Table 7.1. The offset frequency f_0 and the constant distance Δf between tones are set with 100 kHz and 2 kHz, respectively. The signal length and the measurement length must be carefully chosen to have no spectral leakage in the FFT spectrum. In the following experiments, the signal length is set to 1 ms thus the FFT resolution is 1 kHz. The frequencies of the multiple tones as well as the test signals are chosen with 1 kHz resolution so as not to occur the spectral leakage. The spectrum of the pilot signal, which is directly measured at the AWG output with a real-time oscilloscope Keysight DSO-X 93304Q is illustrated in Fig. 7.5. In the zoomed-in view, the single-tone within the single band as defined in Sect. 6.2.1 is clearly seen.

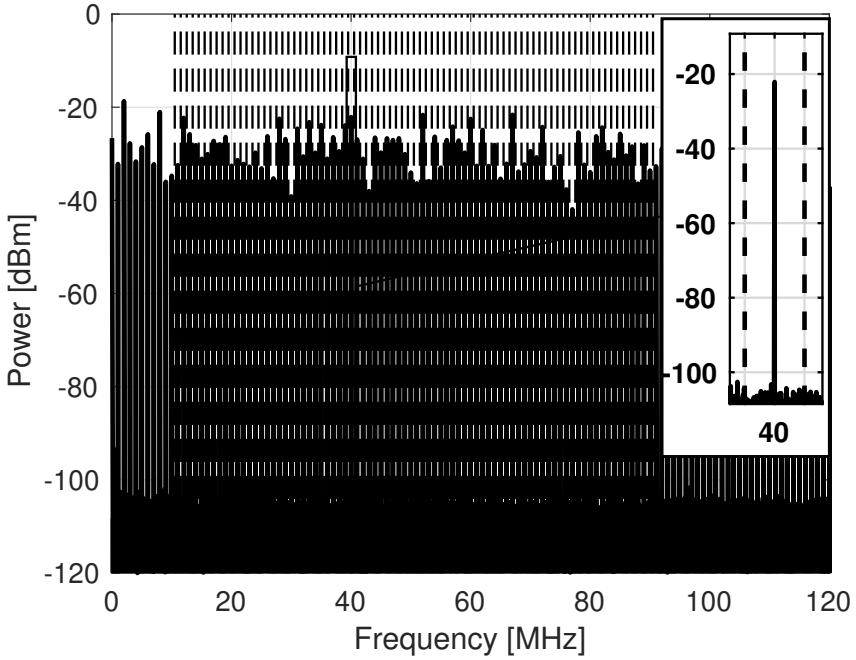

Figure 7.6: Frequency-domain spectrum of the measured PSF signal. In the zoomed-in view, the single-tone resides within the single spectrum slice as shown in Fig. 2.3(a).

b. PSF generation

The PSF is also generated by the AWG. The frequency f_p and the number of symbols M are set as given in Table 7.1. The spectrum of the PSF, which is directly measured at the AWG output is illustrated in Fig. 7.6. The zoomed-in part shows a single component at 40 MHz.

c. Output of the mixer and the LPF

The output spectrum of the mixer at node $\check{y}_i(t)$ in Fig. 7.1 includes the linear combinations of the input spectrum slices $Z_l(f)$ weighted with the corresponding coefficients $c_{i,-l}$ of the PSF as explained in Chapter 2. The spectra at the output of the mixer and the LPF are shown in Figs. 7.7 and 7.8, respectively. The zoomed-in parts show single linear combinations of the input pilot components weighted with PSF coefficients $c_{i,-l}$.

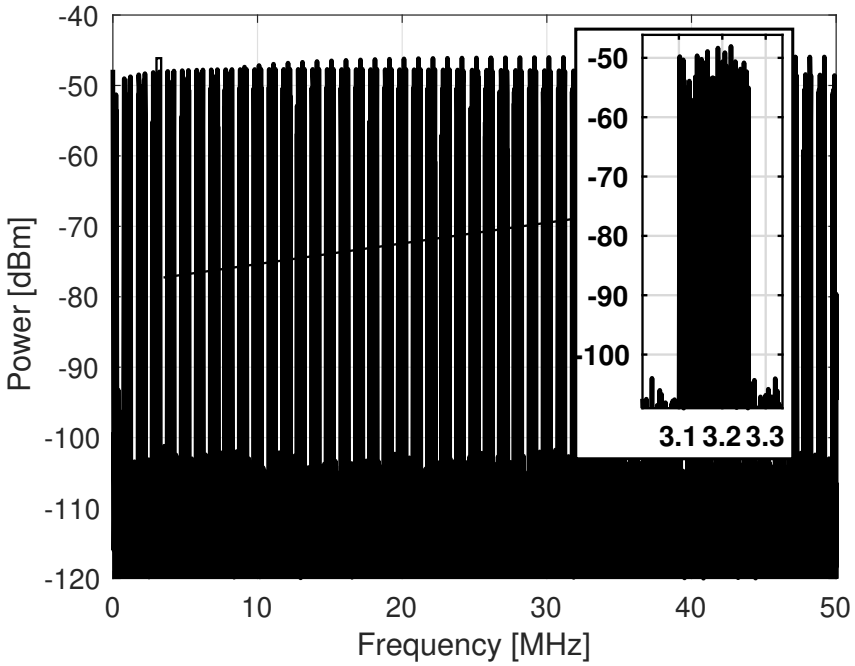

Figure 7.7: Frequency-domain spectrum of the measured mixer output signal. In the zoomed-in view, we can see a linear combinations of the input pilot components weighted with PSF coefficients $c_{i,-l}$.

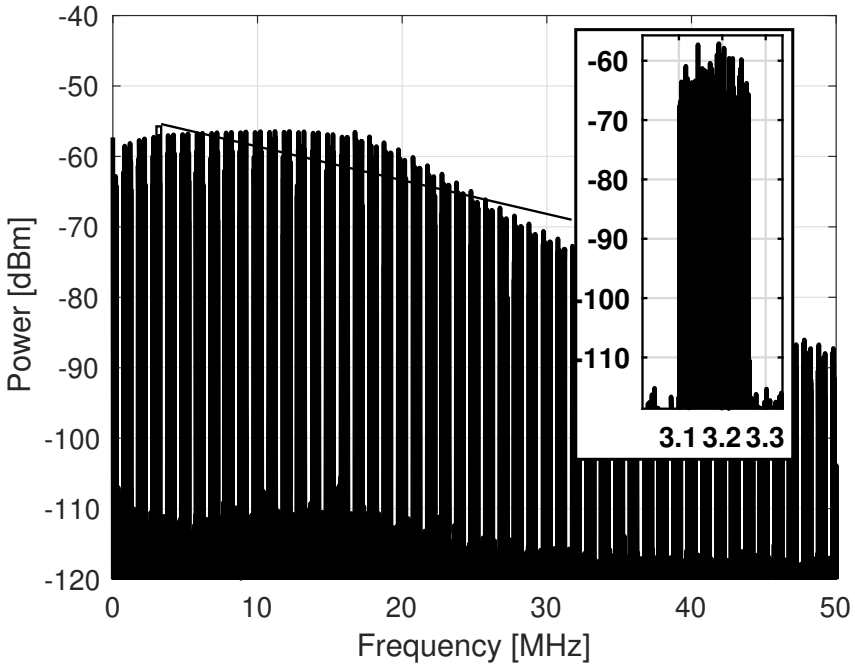

Figure 7.8: Frequency-domain spectrum of the measured LPF output signal. In the zoomed-in view, we can see a linear combinations of the input pilot components weighted with PSF coefficients $c_{i,-l}$.

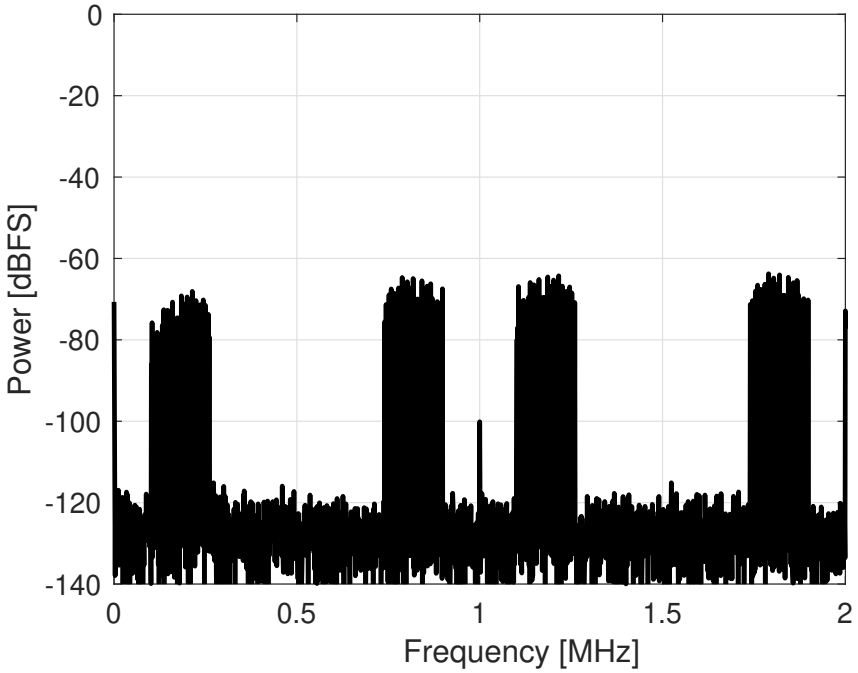

Figure 7.9: A baseband part within 2 MHz of the frequency-domain spectrum for the ADC output signal with the pilot signal

d. Output of the ADC

A baseband part within 2 MHz of the discrete fourier transform (DFT) for the ADC output at node $y_i(t)$ is shown in Fig. 7.9 that includes downconverted PSF coefficients $\tilde{c}_{i,-l}$ at f_l frequencies. At this point, the actual sensing matrix components $\tilde{c}_{i,l}$ can be calculated based on (6.17).

7.3.2 Evaluation of the Calibration Performance

A single-tone signal is used as a test signal after the calibration. The reconstruction performance of the test signal with the calibrated sensing matrix is compared to that with the ideal sensing matrix in terms of NMSE and IRR to evaluate the performance of the proposed calibration method.

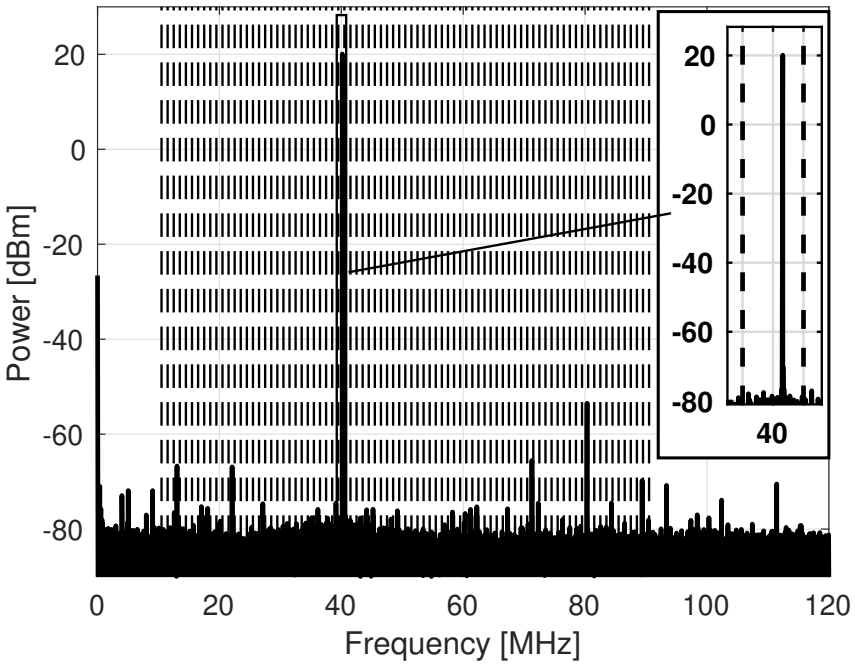

Figure 7.10: Frequency-domain spectrum of the single-tone test signal with 40.16 MHz from the AWG

a. Test signal generation

The single-tone test signal is generated by AWG as an example spectrum with 40.16 MHz is shown in Fig. 7.10. According to the figure, the AWG output itself is not ideal, and some unwanted spurs are originally presented.

b. Reconstruction of the test signal

Firstly, the spectrum of the original test signal with 40.16 MHz directly captured by the real-time oscilloscope is shown in Fig. 7.11(a) and the reconstructed spectrum based on the ideal (uncalibrated) sensing matrix has shown in Fig. 7.11(b) whereas their time-domain waveforms have shown in Figs. 7.11(e) and (f), correspondingly. The uncalibrated matrix causes a large phase error in the reconstructed time-domain waveform that will result in poor NMSE performance. The highlighted circle on the spectrum shows the original single-tone test signal while the triangle depicts the undesired image of the original component that is introduced by the actual sensing matrix deviated from the ideal one. The measured NMSE and IRR were 5.98 dB and 30.05 dB, respectively as summarized in

Table 7.2. The reconstructed spectrum based on the conventional method with sequential single-tone inputs is shown in Fig. 7.11(c) while the time-domain waveform is shown in Fig. 7.11(g). The conventional method needs 80 times measurements while the proposed needs only one. Furthermore, not only the number of measurements is reduced in the proposed method, but also the measurement-to-measurement timing fluctuation in the calibrated sensing matrix is fundamentally suppressed. The measured NMSE and IRR were $-61.53\,\mathrm{dB}$ and $81.63\,\mathrm{dB}$, respectively. The reconstruction based on the proposed calibration method shown in Figs. 7.11(d) and (h) presents the measured NMSE and the IRR of $-66.01\,\mathrm{dB}$ and $82.67\,\mathrm{dB}$, respectively. More than $50\,\mathrm{dB}$ NMSE and $42\,\mathrm{dB}$ IRR improvements are realized by the proposed calibration technique compared to the uncalibrated reconstruction. The spectra and waveforms for $70.22\,\mathrm{MHz}$ test signal based on the uncalibrated, conventional and proposed calibration method are shown in Fig. 7.12. The NMSE and the IRR for this input are also summarized in Table 7.2. The comparison of the IRR and the NMSE performances over the band of interest is shown in Figs. 7.13(a) and (b), respectively. The NMSE and the IRR performances are highly dependent on the carrier frequency due to different coefficients of the PSFs. To make a fair comparison, the average NMSE and the average IRR are calculated in Table 7.2 by taking the average of all NMSE and IRR values for 80 carrier frequencies, correspondingly. The reconstruction based on the ideal (uncalibrated) sensing matrix has poor NMSE and IRR, while the conventional and the proposed calibrations both exhibit excellent performances.

It is worth to point out that the IRR is based only on the amplitude spectrum while the NMSE includes phase differences as well. The main reason that the average IRR of the proposed calibration is lower than the conventional method is that the multi-tone signal does suffer from the non-linearity of the active devices. As discussed in Sect. 6.2.1, the tone frequencies of the pilot signal are defined as linearly spaced frequencies. Therefore, the inter-modulated non-linear components of the linearly spaced frequencies may conflict with its main frequency set, which causes major limitations on the IRR performances. Additionally, the multi-tone signal generated from the AWG has non-linear components

before injected into the MWC. This non-linearity introduces inter-modulation components around the fundamental frequencies and higher-order components into higher frequencies. Some of these components will be downconverted into the same baseband frequencies as the fundamental frequencies and they directly affect the calibration performance. The ADC also introduces non-linearities, which is another contribution to performance degradation. For this reason, a non-linearly spaced frequency set would have better performance. For example, some appropriate subset of the prime numbers can be used as the multi-tone frequencies such that the inter-modulation components of any two-tone differ from the main frequency set. To further improve the IRR performance, devices with higher linearity are recommended. At this moment, it is worth pointing out that the NMSE is more important than IRR because the NMSE includes the phase information that is more important for the time-domain waveform reconstruction applications.

All calibrated coefficients of the sensing matrix through the proposed method do not have any phase error with other coefficients because all the coefficients are obtained from the single measurement. In comparison, the conventional method needs $L/2 = 80$ measurements. In the conventional method, the measurement-to-measurement timing noise is present due to the uncertainty of the ADC sampling time and the synchronous trigger jitter of the AWG even if the calibration setup is fully synchronized. This timing noise can cause different phase deviations on the calibration of the individual coefficients. In contrast, the proposed calibration method inherently does not have the measurement-to-measurement timing noise. For that reason, the phase information is precisely acquired so that the average NMSE has enhanced more than 1 dB from the conventional calibration method as summarized in Table 7.2. In our measurement setup, the synchronous trigger jitter of the AWG was 300 fs, which is negligibly low even for the frequencies of the single-tone calibration method. Therefore the conventional method achieves better IRR performance than the proposed. If we used a signal source with lower timing accuracy or the frequency of interest becomes high, the IRR and the NMSE become unsatisfactory in the conventional method. In summary, the proposed method needs only a single mea-

Table 7.2: The comparison of the reconstruction performances

Reconstruction Methods	Number of calib. meas.	40 MHz		70 MHz		Average	
		NMSE	IRR	NMSE	IRR	NMSE	IRR
Uncalibrated	N/A	5.98	30.05	5.99	30.29	5.96	37.90
Conventional	80	-61.53	81.63	-61.39	83.71	-61.11	84.15
Proposed	1	-66.01	82.67	-63.47	71.84	-62.58	76.42

surement to calibrate all the coefficients of the actual sensing matrix without sacrificing the reconstruction performance, while the conventional method needs time-consuming $L/2$ measurements with phase errors. In addition, even after the calibration measurements, in the conventional method, the subsequent digital processing takes several hours to gather all the coefficients one by one, while the proposed method does not require much computational cost.

7.4 Measurement of Bluetooth Signal

This section is removed in this abridged version.

7.5 Power Consumption of the MWC

This section is removed in this abridged version.

7.6 Summary

This chapter proposed the novel calibration technique for the MWC to estimate its actual sensing matrix coefficients with single measurements. In terms of the calibration time, the proposed calibration technique exploits only a single measurement, while the conventional calibration method repeats several measurements with single-tone inputs. For this implementation setup, the previous calibration as in Sect. 6.1 would need 80 measurements and the digital processing would be much more complicated than the proposed method. The decrease in the number of calibration measurements reduces the effect of the timing noise

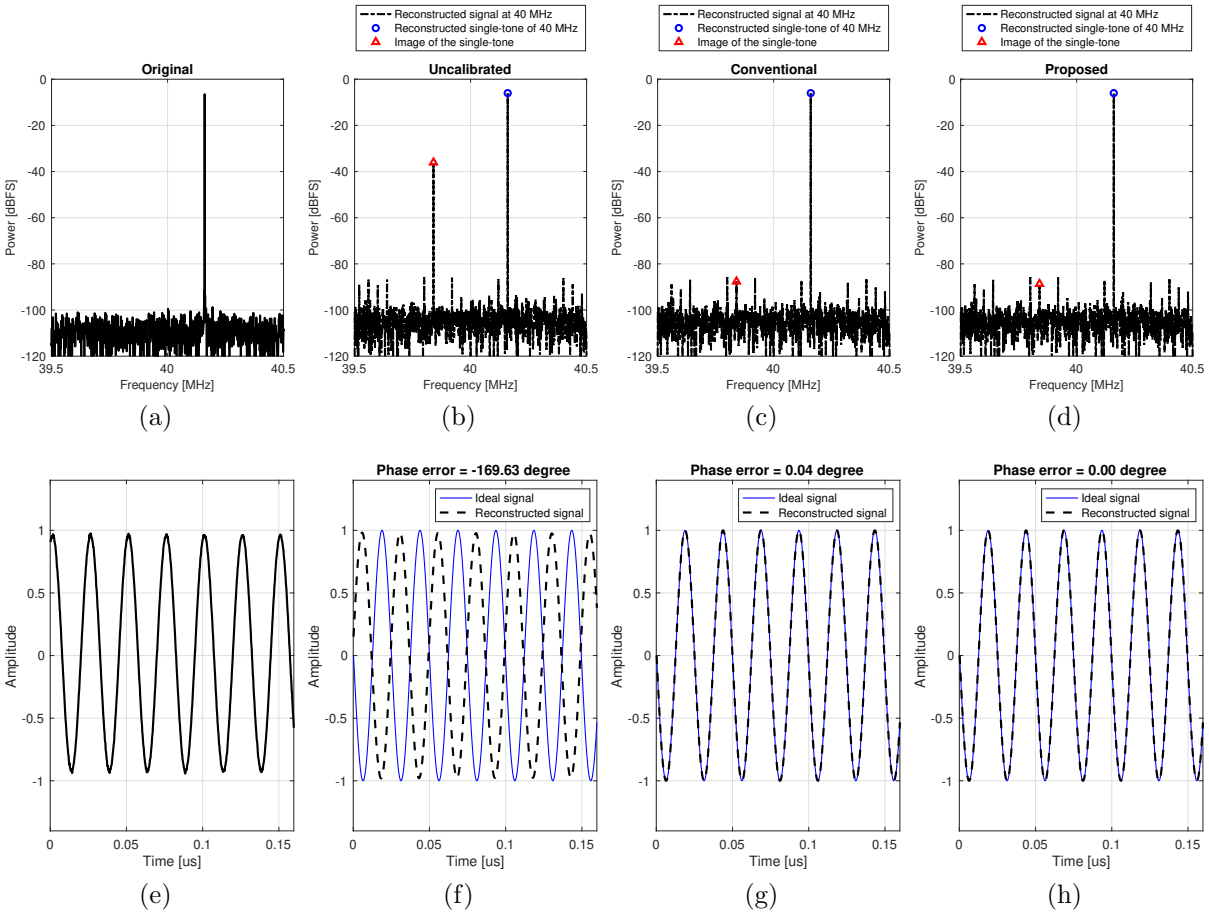

Figure 7.11: Frequency-domain spectrum of (a) the input single-tone test signal with 40.16 MHz directly measured with a real-time oscilloscope, (b) the reconstructed signal based on the uncalibrated ideal **A** matrix, (c) that based on the calibrated **A** matrix constructed by the conventional method and (d) that based on the calibrated **A** matrix constructed by the proposed method. (e) Time-domain waveform of the first few periods of the input single-tone test signal, (f) the reconstructed single-tone test signal based on the uncalibrated ideal **A** matrix, (g) that based on the calibrated **A** matrix constructed by the conventional method and (h) that based on the calibrated **A** matrix constructed by the proposed method.

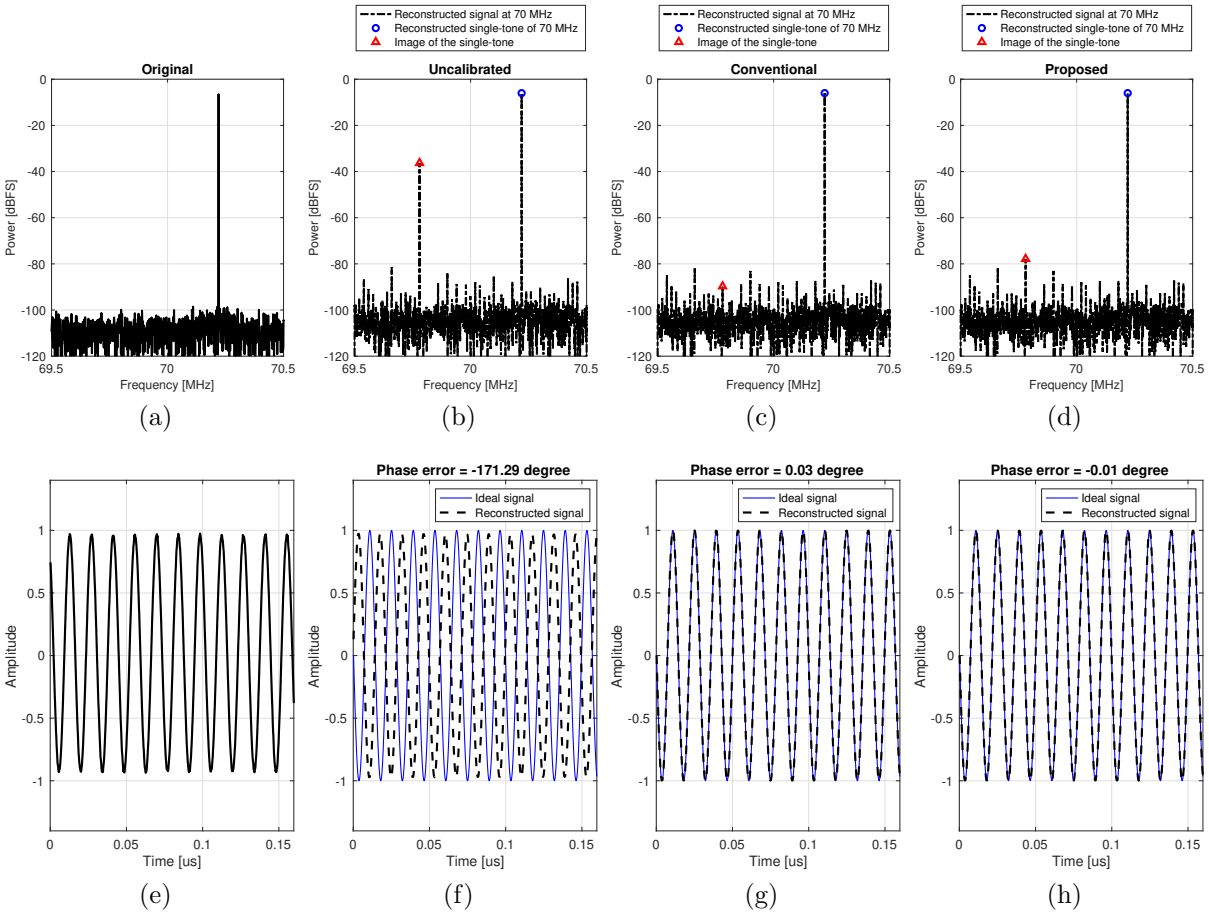

Figure 7.12: Frequency-domain spectrum of (a) the input single-tone test signal with 70.22 MHz directly measured with a real-time oscilloscope, (b) the reconstructed signal based on the uncalibrated ideal **A** matrix, (c) that based on the calibrated **A** matrix constructed by the conventional method and (d) that based on the calibrated **A** matrix constructed by the proposed method. (e) Time-domain waveform of the first few periods of the input single-tone test signal, (f) the reconstructed single-tone test signal based on the uncalibrated ideal **A** matrix, (g) that based on the calibrated **A** matrix constructed by the conventional method and (h) that based on the calibrated **A** matrix constructed by the proposed method.

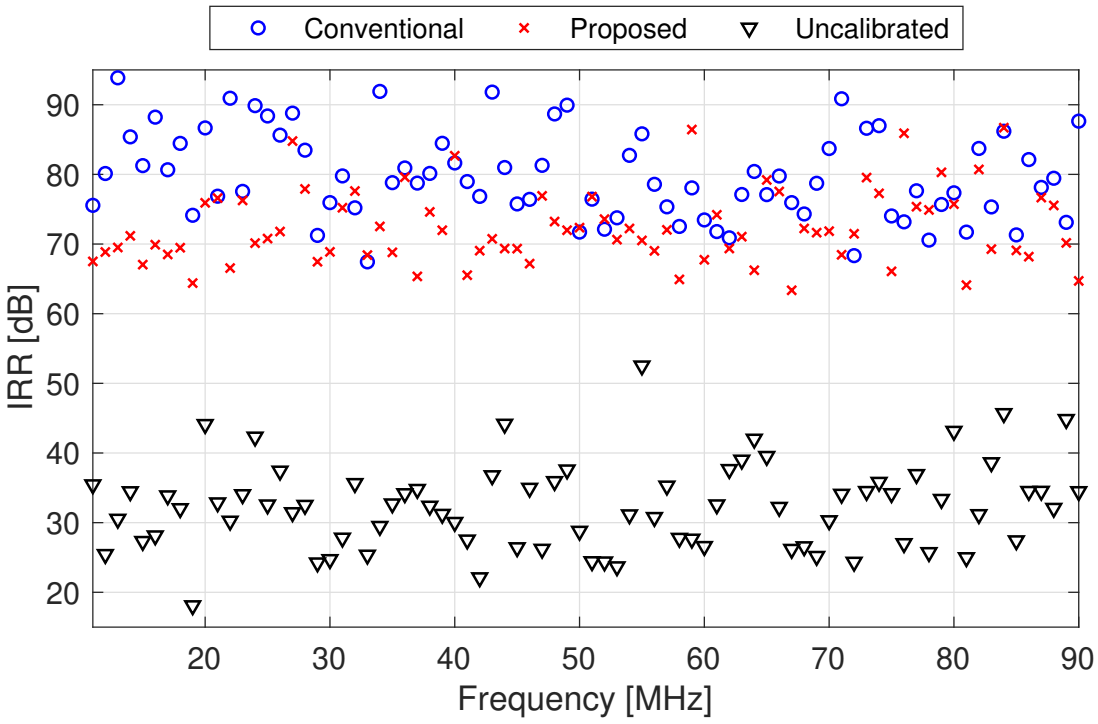

(a)

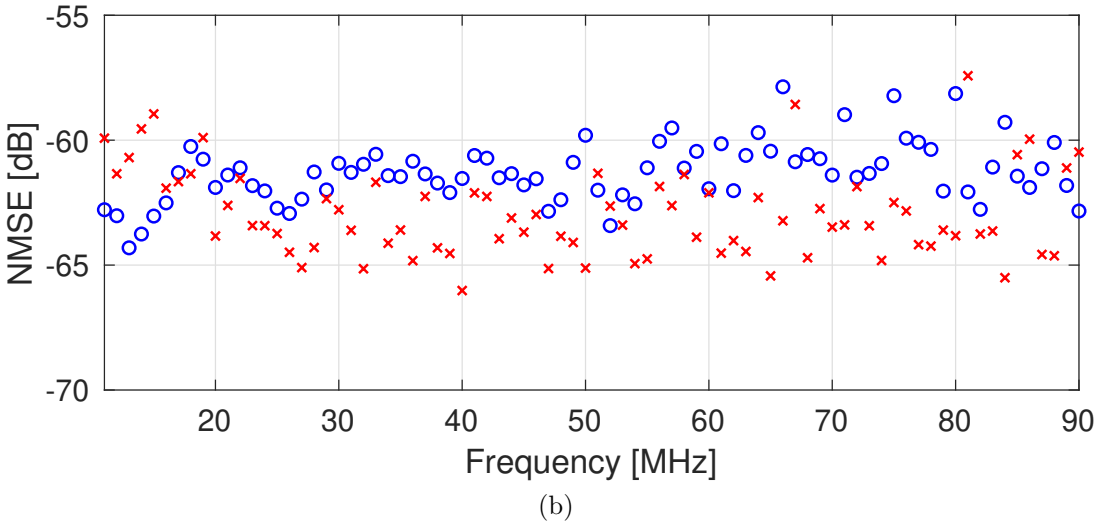

(b)

Figure 7.13: The comparisons of (a) IRR and (b) NMSE performances for the frequencies over the band of interest.

in the calibrated matrix and the computation task in the digital domain compared to the conventional method. The calibration performance has been demonstrated in NMSE and IRR, more than 50 dB and 42 dB improvement has been achieved on NMSE and IRR, respectively.

Chapter 8

Conclusions

This thesis focused on analysis and calibration techniques of the modulated wideband converter (MWC) for a high-precision sub-Nyquist sampling system. We addressed theoretical analysis of the noise figure for the MWC to facilitate the system-level optimization of the MWC-based receiver architectures in terms of noise performance. The noise figure of the MWC strongly depends on the carrier position of the input signal due to the unlikeness of the Fourier series coefficients of the PSF. The simulation result shows that the analytic noise figure successfully estimates the simulated NF of MWC, created with different design parameters. In the practical case, as the sampling rate and the number of channels are limited, most MWC-based applications such as spectrum analyzer and cognitive radio have a great interest in the region $m \ll L$. Even though the noise figure of the MWC becomes considerably high when $m \ll L$, with an appropriate choice of low-NF, high-gain RF front-end circuits, the overall noise figure can be reduced to target specification. The proposed theoretical analysis on NF of the MWC systems will facilitate the system-level optimization of the MWC-based receiver architectures in terms of noise performance. The choice of the PSF determines the worthiness of the sensing matrix. In other words, the PSF decides the NF of the particular carrier location of the input signal. Thus the remaining challenge in the topic is how to build the PSFs with minimized noise figures.

The simulation results obtained from our created MWC platform on MATLAB show

that the time-domain waveform reconstruction can be correctly done under ideal situations. When the wideband signal is not clean sparse, the sidebands should also be considered for the reconstruction to improve the performance.

We proposed a novel calibration method for simultaneous estimation of all the actual sensing matrix components based on a single measurement with a non-sparse multi-tones signal. Not only the number of measurements is reduced in the proposed method, but also the impact of the measurement-to-measurement timing fluctuations on the calibrated sensing matrix is fundamentally suppressed.

We demonstrated the measurement results of the MWC taken from the practical implementation. The measurement result of the noise figure in MWC validates the correctness of the theoretical noise analysis. The proposed calibration technique for the MWC estimated the actual sensing matrix coefficients with single measurements while the conventional calibration needs many measurements. The calibration performance has been demonstrated in NMSE and IRR compared to the uncalibrated performance, more than 50 dB and 42 dB improvement has been achieved on NMSE and IRR, respectively. If the non-linearity of the circuits is significant, the frequency set of the proposed calibration should be obtained by the algorithm to make it robust for the non-linearity.

In terms of power consumption in the implementation, the total power consumption of the 4-channel MWC was 4.82 W while a single off-the-shelf ADC can obtain the same total sampling rate with 2.5 W. However, the MWC can be an impressive choice for some applications which use a multiband sparse signal around a few GHz. In those applications, the MWC can reduce the sampling rate of the ADC to improve the precision by utilizing multi-channel, while a single ADC with a high sampling rate consumes more power and suffers on the precision. The dominant part of the total power consumption is undoubtedly the active mixer. The custom-designed switching type mixer should be made to reduce the power consumption more.

The presented work in the thesis improves the overall performance of the MWC reconstruction, especially in practical implementations. There are numerous application fields

that the MWC can be used. One of those fields is automatic test equipment (ATE) for wireless device testing. Using the sparsity of the wireless signals, the MWC can efficiently capture the analog information into the digital domain. In the ATE environment, there are many low sampling rate high-precision ADCs, which is a perfect place to exploit the MWC. Because utilizing existing components is very important for the ATE in terms of cost. Based on the results throughout the thesis, the practical implementation of MWC can be done in a straight-forwarding way. Confirming the MWC performance more to broaden the application area, the performance of the MWC reconstruction with an orthogonal frequency-division multiplexing (OFDM) modulated signal should be done to measure Long Term Evolution (LTE) standardized signals in the future.

Bibliography

[1] J. Mitola. Software radios-survey, critical evaluation and future directions. In *[Proceedings] NTC-92: National Telesystems Conference*, pages 13/15–13/23, May 1992.

[2] S. Haykin. Cognitive radio: brain-empowered wireless communications. *IEEE Journal on Selected Areas in Communications*, 23(2):201–220, Feb 2005.

[3] K. Entesari and P. Sepidband. Spectrum sensing: Analog (or partially analog) CMOS real-time spectrum sensing techniques. *IEEE Microwave Magazine*, 20(6):51–73, June 2019.

[4] M. Kim and J. Takada. Efficient multi-channel wideband spectrum sensing technique using filter bank. In *2009 IEEE 20th International Symposium on Personal, Indoor and Mobile Radio Communications*, pages 1014–1018, Sep. 2009.

[5] H. Sun, A. Nallanathan, C. Wang, and Y. Chen. Wideband spectrum sensing for cognitive radio networks: a survey. *IEEE Wireless Communications*, 20(2):74–81, April 2013.

[6] M. Mishali and Y. C. Eldar. Sub-Nyquist sampling. *IEEE Signal Processing Magazine*, 28(6):98–124, Nov 2011.

[7] M. Mishali and Y. C. Eldar. From theory to practice: Sub-Nyquist sampling of sparse wideband analog signals. *IEEE Journal of Selected Topics in Signal Processing*, 4(2):375–391, April 2010.

[8] M. Mishali and Y. C. Eldar. Blind multiband signal reconstruction: Compressed sensing for analog signals. *IEEE Transactions on Signal Processing*, 57(3):993–1009, March 2009.

[9] M. Mishali, Y. C. Eldar, O. Dounaevsky, and E. Shoshan. Xampling: Analog to digital at sub-Nyquist rates. *IET Circuits, Devices Systems*, 5(1):8–20, January 2011.

[10] D. Adams, Y. Eldar, and B. Murmann. A mixer frontend for a four-channel modulated wideband converter with 62 dB blocker rejection. In *2016 IEEE Radio Frequency Integrated Circuits Symposium (RFIC)*, pages 286–289, May 2016.

[11] D. Adams, Y. C. Eldar, and B. Murmann. A mixer front end for a four-channel modulated wideband converter with 62-dB blocker rejection. *IEEE Journal of Solid-State Circuits*, 52(5):1286–1294, May 2017.

[12] M. Mishali and Y. C. Eldar. Blind multiband signal reconstruction: Compressed sensing for analog signals. *IEEE Transactions on Signal Processing*, 57(3):993–1009, March 2009.

[13] J. Park, J. Jang, and H. Lee. A calibration for the modulated wideband converter using sinusoids with unknown phases. In *2017 Ninth International Conference on Ubiquitous and Future Networks (ICUFN)*, pages 951–955, July 2017.

[14] Weisong Liu, Zhitao Huang, Xiang Wang, and Weichao Sun. Design of a single channel modulated wideband converter for wideband spectrum sensing: Theory, architecture and hardware implementation. *Sensors*, 17:1035, 05 2017.

[15] E. Israeli, S. Tsiper, D. Cohen, E. Shoshan, R. Hilgendorf, A. Reysenson, and Y. C. Eldar. Hardware calibration of the modulated wideband converter. In *2014 IEEE Global Communications Conference*, pages 948–953, Dec 2014.

[16] Y. C. Pati, R. Rezaiifar, and P. S. Krishnaprasad. Orthogonal matching pursuit: recursive function approximation with applications to wavelet decomposition. In *Pro-*

ceedings of 27th Asilomar Conference on Signals, Systems and Computers, pages 40–44 vol.1, Nov 1993.

[17] D. L. Donoho. Compressed sensing. *IEEE Transactions on Information Theory*, 52(4):1289–1306, April 2006.

[18] E. J. Candes, J. Romberg, and T. Tao. Robust uncertainty principles: exact signal reconstruction from highly incomplete frequency information. *IEEE Transactions on Information Theory*, 52(2):489–509, Feb 2006.

[19] M. Mishali and Y. C. Eldar. Reduce and boost: Recovering arbitrary sets of jointly sparse vectors. *IEEE Transactions on Signal Processing*, 56(10):4692–4702, Oct 2008.

[20] E. J. Candes and T. Tao. Decoding by linear programming. *IEEE Transactions on Information Theory*, 51(12):4203–4215, Dec 2005.

[21] David L. Donoho and Michael Elad. Optimally sparse representation in general (nonorthogonal) dictionaries via l1 minimization. *Proceedings of the National Academy of Sciences*, 100(5):2197–2202, 2003.

[22] Moshe Rosenfeld. *In Praise of the Gram Matrix*, pages 318–323. Springer Berlin Heidelberg, Berlin, Heidelberg, 1997.

[23] N. Kurosawa, H. Kobayashi, K. Maruyama, H. Sugawara, and K. Kobayashi. Explicit analysis of channel mismatch effects in time-interleaved adc systems. *IEEE Transactions on Circuits and Systems I: Fundamental Theory and Applications*, 48(3):261–271, March 2001.

[24] R. T. Yazicigil, T. Haque, M. R. Whalen, J. Yuan, J. Wright, and P. R. Kinget. Wideband rapid interferer detector exploiting compressed sampling with a quadrature analog-to-information converter. *IEEE Journal of Solid-State Circuits*, 50(12):3047–3064, Dec 2015.

[25] T. Haque, R. T. Yazicigil, K. J. Pan, J. Wright, and P. R. Kinget. Theory and design of a quadrature analog-to-information converter for energy-efficient wideband spectrum sensing. *IEEE Transactions on Circuits and Systems I: Regular Papers*, 62(2):527–535, Feb 2015.

[26] R. T. Yazicigil, T. Haque, M. Kumar, J. Yuan, J. Wright, and P. R. Kinget. A compressed-sampling time-segmented quadrature analog-to-information converter for wideband rapid detection of up to 6 interferers with adaptive thresholding. In *2016 IEEE Radio Frequency Integrated Circuits Symposium (RFIC)*, pages 282–285, May 2016.

[27] A. Harms, W. U. Bajwa, and R. Calderbank. A constrained random demodulator for sub-nyquist sampling. *IEEE Transactions on Signal Processing*, 61(3):707–723, 2013.

[28] D. Karampoulas, L. S. Dooley, and S. K. Mostefaoui. Unified compressive sensing paradigm for the random demodulator and compressive multiplexer architectures. *IET Signal Processing*, 14(8):513–521, 2020.

[29] M. Mashhour and A. I. Hussein. Sub-Nyquist wideband spectrum sensing based on random demodulation in cognitive radio. In *2017 12th International Conference on Computer Engineering and Systems (ICCES)*, pages 712–716, 2017.

[30] Keith Godfrey, editor. *Perturbation Signals for System Identification*. Prentice Hall International (UK) Ltd., GBR, 1993.

[31] M. Schroeder. Synthesis of low-peak-factor signals and binary sequences with low autocorrelation (corresp.). *IEEE Transactions on Information Theory*, 16(1):85–89, January 1970.

[32] S. Boyd. Multitone signals with low crest factor. *IEEE Transactions on Circuits and Systems*, 33(10):1018–1022, October 1986.

[33] H. T. Friis. Noise figures of radio receivers. *Proceedings of the IRE*, 32(7):419–422, July 1944.

[34] The modulated wideband converter: Sub-Nyquist sampling of sparse wideband analog signals. `http://webee.technion.ac.il/people/YoninaEldar/software\_det2.php`. Accessed: 2019-08-20.

[35] M. A. Davenport, J. N. Laska, J. R. Treichler, and R. G. Baraniuk. The pros and cons of compressive sensing for wideband signal acquisition: Noise folding versus dynamic range. *IEEE Transactions on Signal Processing*, 60(9):4628–4642, Sep. 2012.

[36] Peng Wang, Fei You, and Songbai He. An improved signal reconstruction of modulated wideband converter using a sensing matrix built upon synchronized modulated signals. *Circuits, Systems, and Signal Processing*, 38(7):3187–3210, Jul 2019.

[37] N. Fu, S. Jiang, L. Deng, and L. Qiao. Successive-phase correction calibration method for modulated wideband converter system. *IET Signal Processing*, 13(6):624–632, 2019.

[38] P. Wang, F. You, and S. He. Design of broadband compressed sampling receiver based on concurrent alternate random sequences. *IEEE Access*, 7:135525–135538, 2019.

[39] F. You, P. Shang, and P. Wang. Design of a low-cost integrated RF front-end for a modulated-wideband-converter based receiver. In *2017 IEEE Asia Pacific Microwave Conference (APMC)*, pages 1099–1102, Nov 2017.

[40] M. Mishali and Y. C. Eldar. Wideband spectrum sensing at sub-Nyquist rates [applications corner]. *IEEE Signal Processing Magazine*, 28(4):102–135, July 2011.

[41] M. Mishali, Y. C. Eldar, O. Dounaevsky, and E. Shoshan. Xampling: Analog to digital at sub-Nyquist rates. *IET Circuits, Devices Systems*, 5(1):8–20, January 2011.

[42] Yijiu Zhao, Yu Hen Hu, and Jingjing Liu. Random triggering based sub-Nyquist sampling system for sparse multiband signal. *CoRR*, abs/1703.01933, 2017.

[43] R. T. Yazicigil, T. Haque, M. R. Whalen, J. Yuan, J. Wright, and P. R. Kinget. Wideband rapid interferer detector exploiting compressed sampling with a quadrature

analog-to-information converter. *IEEE Journal of Solid-State Circuits*, 50(12):3047–3064, 2015.

[44] R. T. Yazicigil, T. Haque, M. Kumar, J. Yuan, J. Wright, and P. R. Kinget. A compressed-sampling time-segmented quadrature analog-to-information converter for wideband rapid detection of up to 6 interferers with adaptive thresholding. In *2016 IEEE Radio Frequency Integrated Circuits Symposium (RFIC)*, pages 282–285, 2016.

[45] T. Haque, R. T. Yazicigil, K. J. Pan, J. Wright, and P. R. Kinget. Theory and design of a quadrature analog-to-information converter for energy-efficient wideband spectrum sensing. *IEEE Transactions on Circuits and Systems I: Regular Papers*, 62(2):527–535, 2015.

[46] L. Chen, J. Jin, and Y. Gu. A calibration system and perturbation analysis for the modulated wideband converter. In *IEEE 10th INTERNATIONAL CONFERENCE ON SIGNAL PROCESSING PROCEEDINGS*, pages 78–81, Oct 2010.

[47] Y. K. Alp, A. B. Korucu, A. T. Karabacak, A. C. G‘rb‘z, and O. Ar‘kan. Online calibration of modulated wideband converter. In *2016 24th Signal Processing and Communication Application Conference (SIU)*, pages 913–916, May 2016.

[48] P. Welch. The use of fast Fourier transform for the estimation of power spectra: A method based on time averaging over short, modified periodograms. *IEEE Transactions on Audio and Electroacoustics*, 15(2):70–73, 1967.

[49] S. Boyd. Multitone signals with low crest factor. *IEEE Transactions on Circuits and Systems*, 33(10):1018–1022, October 1986.

[50] N. Dong and J. Wang. Channel gain mismatch and time delay calibration for modulated wideband converter-based compressive sampling. *IET Signal Processing*, 8(2):211–219, April 2014.

[51] Datasheet ADL5801. (Date last accessed 9-Feb-2020).

[52] Datasheet LTC6604. (Date last accessed 9-Feb-2020).

[53] Datasheet LTC2207. (Date last accessed 9-Feb-2020).

List of Publications

Journal Papers

[1] Z. Byambadorj, K. Asami, T. J. Yamaguchi, A. Higo, M. Fujita, and T. Iizuka. Theoretical analysis of noise figure for modulated wideband converter. *IEEE Transactions on Circuits and Systems I: Regular Papers*, 67(1):298–308, Jan 2020.

[2] Z. Byambadorj, K. Asami, T. J. Yamaguchi, A. Higo, M. Fujita, and T. Iizuka. A calibration technique for simultaneous estimation of actual sensing matrix coefficients on modulated wideband converters. *IEEE Transactions on Circuits and Systems I: Regular Papers*, pages 1–13, 2020 *(Early Access)*.

Proceedings of International Conferences

[1] Z. Byambadorj, K. Asami, T. J. Yamaguchi, A. Higo, M. Fujita, and T. Iizuka. Theoretical analysis on noise performance of modulated wideband converters for analog testing. In *2020 26th Asian Test Symposium (ATS)*, Nov 2020.

Patents

[1] Zolboo Byambadorj, Koji Asami, and Tetsuya Iizuka. Calibration techniques for compressed sensing circuits. Japan Patent Application No. 2020-76379.